INTERNATIONAL JOURNAL FOR NUMERICAL METHODS IN FLUIDS, VOL. 17, 417–445 (1993)

SHALLOW FLOW MODELLING USING CURVILINEAR DEPTH-AVERAGED STREAM FUNCTION AND VORTICITY TRANSPORT EQUATIONS

A. G. L. BORTHWICK AND E. T. KAAR
Department of Engineering Science, University of Oxford, Parks Road, Oxford OX1 3PJ, U.K.

SUMMARY

Most receiving waters, such as lakes and open reservoirs, have large plan dimensions with respect to their depth. In such cases, the flow may be nearly two-dimensional and the depth-averaged Reynolds equations are appropriate. This paper presents a new version of the governing equations in curvilinear depth-averaged stream function and vorticity transport (ψ, ω) form appropriate for non-orthogonal computational meshes. The equations are discretized using finite differences and solved using successive over-relaxation for the depth-averaged stream function equation and an alternating direction implicit scheme for the vorticity transport equation. Results from the numerical model are validated against data from flow past a backward-facing step and jet-forced flow in a circular reservoir. The results indicate that the (ψ, ω) form of the shallow water equations may be useful for applications where the free surface can either be assumed horizontal, or is known *a priori*.

KEY WORDS Computational hydraulics Shallow water equations Non-orthogonal curvilinear systems

INTRODUCTION

Water engineers often deal with separated, free-surface flows where the depth is relatively shallow compared with the horizontal dimensions. In cases of wide rivers and lakes where vertical stratification effects are negligible and bed processes, such as sediment transport, are not under consideration, it is reasonable to use the depth-averaged Reynolds equations (otherwise known as the shallow water equations) to model the flow behaviour.

Perhaps the first operational estuarine hydrodynamic model based on the shallow water equations was developed by Leendertse,[1] who used a semi-implicit (alternating direction implicit) technique on a two-dimensional (2D) space-staggered mesh. Leendertse[2] extended the hydrodynamic model to incorporate water quality simulation in estuaries and coastal seas. Many subsequent models have been based on Leendertse's scheme. Kuipers and Vreugdenhil[3] computed steady 2D flow patterns using Leendertse's scheme, paying particular attention to secondary flow phenomena. Using the same scheme, Vreugdenhil and Wijbenga[4] modelled flow patterns in rivers, using the results to judge the effects of diking and dredging in the flood plains of the Dutch river system. The shallow water equations were solved for flow in open channels by Rastogi and Rodi.[5] They included a depth-averaged k–ε turbulence model and then extended the hydrodynamics to predict heat and mass transfer. Various authors have examined phase problems which can arise when semi-implicit (alternating direction implicit) schemes are applied to cases involving irregular boundaries. Wolf[6] reported that alternating direction implicit (ADI)

0271-2091/93/170417-29$19.50

Received November 1992
Revised April 1993

schemes lose symmetry at closed boundaries and wherever velocities are specified. With reference to a fine-grid model of the Bristol Channel, Wolf emphasised that dissipation and instabilities were created at corners of the stepped boundary, before diffusing into the interior solution. Stelling *et al.*[7] demonstrated that the numerical propagation speed of waves in an ADI scheme depends not only on the time step and grid size, but also on the geometry and bathymetry. They found that the Courant number must be restricted to no more than $4\sqrt{2}$ in order for a wave to propagate properly through a zig-zag channel (i.e. along an irregular stepped boundary). Similar problems arise with ADI schemes in the case of bathymetric irregularities, as discussed by Wilders *et al.*[8] for the case of a rectangular basin containing a deep S-shaped channel. Wilders *et al.*[8] proposed a fully implicit scheme which utilized the conjugate gradients squared method and eliminated the foregoing geometrical phase effects.

Although the majority of shallow flow solvers have been based on finite difference discretization, finite element procedures and the method of characteristics have been utilized successfully. Taylor and Davies[9] and Faraday *et al.*[10] employed a finite element scheme to calculate 2D flows in estuaries. Lai[11] utilized the method of characteristics for advection terms and simulated flow in a hypothetical bay. Benqué *et al.*[12] produced an efficient method for computing tide-generated currents by solving advection by the method of characteristics, diffusion by an alternating direction implicit (ADI) approach and linearized wave propagation terms by a modified iterative alternating direction procedure.

Rather less literature is available concerning the shallow water equations in mapped or curvilinear form. Boericke and Hall[13] used algebraic translations to map the irregular shorelines of an estuary onto a rectangular co-ordinate space. Johnson and Thompson[14] presented non-orthogonal boundary-fitted (curvilinear) versions of the vertically integrated equations of motion and sediment transport. Johnson[15] solved the non-orthogonal shallow water equations written in terms of Cartesian primitive variables (i.e. depth-averaged velocity components and surface elevation) using a semi-implicit finite difference scheme and tested it on an idealized estuary. Using a fully implicit scheme, Sheng and Hirsh[16] solved the non-orthogonal shallow water equations with contravariant velocity components and compared predictions of wind-driven and tidal circulations with analytical solutions. Spaulding[17] predicted the M_2 tidal-induced circulation in the North Sea using a semi-implicit non-orthogonal curvilinear formulation of the vertically averaged shallow sea equations. For validation purposes, Spaulding also considered tidal forcing in an exponential frictionless channel, long waves in a wedge-shaped basin, and wind-induced set-up in a complex basin. Willemse *et al.*[18] used a stable, semi-implicit finite difference procedure devised by Stelling[19] to solve the orthogonal shallow water equations. Orthogonal systems have the advantage that the transformed equations are simpler than the corresponding non-orthogonal expressions, but the constraint of orthogonality reduces flexibility in determining grid point distribution, especially at the boundary. Wijbenga[20] used a similar orthogonal grid to calculate flood levels and flow patterns in the Waal and Ijssel rivers. Häuser *et al.*[21] and Raghunath *et al.*[22] solved the linearized shallow water equations in non-orthogonal form by integrating the Cartesian velocity components and surface elevations on two staggered meshes. They compared predictions with analytical solutions of flows in a circular ring and rotating cylindrical containers. Recently, Borthwick and Barber[23] obtained solutions of the full shallow water equations for uniform flow in a rectangular channel and jet-forced flow in a circular reservoir. They employed a semi-implicit, finite difference scheme on a single staggered mesh. Hervoulet[24] used a combination of the method of characteristics for advection and finite elements for diffusion and propagation to solve the curvilinear shallow water equations. Predictions were compared with classical analytical solutions, experimental data and field measurements, before calculating backwater effects due to bridges.

The depth-averaged stream function and vorticity-transport (ψ, ω) equations provide a viable alternative to the primitive-variable versions of the shallow water equations. In effect, the three-equation primitive-variable system is reduced to two equations by the elimination of the pressure term in the momentum equations through cross-differentiation and subtraction. Solution of the (ψ, ω) system may be carried out efficiently as a combination of initial and boundary value problems on a non-staggered mesh. The (ψ, ω) approach has a serious disadvantage in that the boundary conditions are not always straightforward to specify, especially as values of depth-averaged vorticity are not easy to interpret intuitively. In addition, it is assumed that surface slopes are small and that the amplitude of gravity waves is unimportant.

Very few references can be found to spatially discretized depth-averaged stream function and vorticity transport models. Codell[25] solved for ψ and ω using a time-stepping alternating direction implicit scheme on a staggered grid and simulated flow near a hypothetical power plant intake. Chalmers[26] and Ball *et al.*[27] used the depth-averaged (ψ, ω) equations in Cartesian form to compute flow fields around estuarine structures. As far as can be ascertained, there are no references for the solution of the depth-averaged (ψ, ω) equations in curvilinear form. However, Oliver and Miller[28] produced a model for predicting 2D, steady-state flows and heat transfer by solving the non-depth-averaged 2D non-orthogonal stream function and vorticity transport equations. They tested their model against well-documented flows such as forced convection in parallel plate ducts and natural convection in a concentric annulus.

In this paper, the depth-averaged (ψ, ω) equations are derived and a computational solution procedure outlined. Results from two series of validation tests are presented: first, the depth-averaged (ψ, ω) solver is used to simulate laminar flow past a backward-facing step in a rectangular channel and predictions compared with experimental and other numerical results. The test enables an assessment to be made of the level of artificial viscosity in the scheme within the range of Reynolds numbers considered. Second, in order to examine the effect of terms relating to grid curvature, the depth-averaged (ψ, ω) program simulated jet-forced flow in a circular reservoir.

GOVERNING EQUATIONS

The Reynolds equations express time-averaged conservation of mass and momentum of a Newtonian fluid and may be reduced to a 2D form appropriate to relatively shallow (vertically mixed) flows by integrating over the vertical dimension, z. The integration takes place from the bed, $z = -h$, to the free surface, $z = \zeta$, defined in Figure 1, and all parameters are expressed in terms of depth-averaged values. A major assumption is that vertical fluid accelerations are negligible compared with gravity. Consequently, a hydrostatic pressure distribution is established, and, by neglecting gradients of atmospheric pressure at the free surface, the gradients of mean pressure $\partial p/\partial x$ and $\partial p/\partial y$ are directly proportional to $\partial \zeta/\partial x$ and $\partial \zeta/\partial y$.

We define the depth-averaged velocities, U and V, as

$$U = \frac{1}{D}\int_{-h}^{\zeta} u \,\mathrm{d}z \quad \text{and} \quad V = \frac{1}{D}\int_{-h}^{\zeta} v \,\mathrm{d}z \,, \tag{1}$$

where D is the total water depth $(D = h + \zeta)$, and u and v are temporal mean velocity components acting in the x- and y-directions, respectively. Integration of the Reynolds equations and application of the Leibnitz rule with appropriate boundary conditions for the surface and bed, yield the depth-averaged mass and momentum equations (Reference 3) as

$$\frac{\partial D}{\partial t} + \frac{\partial (UD)}{\partial x} + \frac{\partial (VD)}{\partial y} = 0 \,, \tag{2a}$$

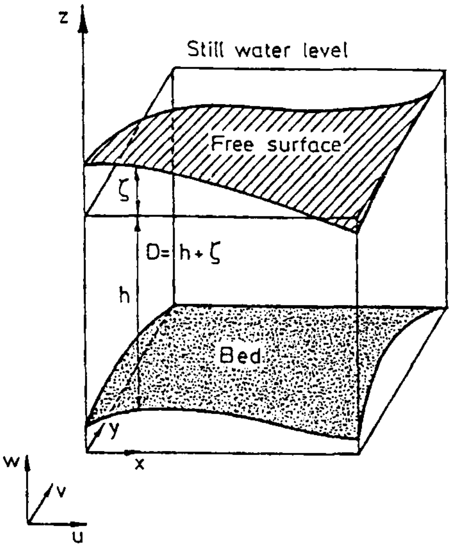

Figure 1. Definition sketch

$$\frac{\partial U}{\partial t}+U\frac{\partial U}{\partial x}+V\frac{\partial U}{\partial y}-fV+g\frac{\partial \zeta}{\partial x}-\frac{1}{\rho D}(\tau_{wx}-\tau_{bx})-\frac{1}{\rho D}\left[\frac{\partial (DT_{xx})}{\partial x}+\frac{\partial (DT_{xy})}{\partial y}\right]=0 \qquad \text{(2b)}$$

and

$$\frac{\partial V}{\partial t}+U\frac{\partial V}{\partial x}+V\frac{\partial V}{\partial y}+fU+g\frac{\partial \zeta}{\partial y}-\frac{1}{\rho D}(\tau_{wy}-\tau_{by})-\frac{1}{\rho D}\left[\frac{\partial (DT_{xy})}{\partial x}+\frac{\partial (DT_{yy})}{\partial y}\right]=0. \qquad \text{(2c)}$$

The above shallow water equations conserve mass and momentum in terms of the depth-averaged horizontal velocities U and V. In equations (2), f is the Coriolis parameter ($f=2\Omega\sin\theta$, where Ω is the angular velocity of the Earth and θ is the geographic latitude), τ_{bx} and τ_{by} are components of bottom frictional shear stress, τ_{wx} and τ_{wy} are components of the surface stress (due to wind), g is the acceleration due to gravity, and ρ is fluid density. Deviatoric fluid stresses and terms resulting from integration over depth are grouped together (as in Reference 3) to give the so-called effective stresses T_{xx}, T_{xy}, T_{yy}. In its raw state, each effective stress is made up of three distinct parts. The first is a laminar viscous contribution and may be judged negligible in turbulent flow regimes. The second term represents turbulent stresses which arise from the time-averaging procedure. The third results from integration over the depth and describes momentum transport due to non-uniform vertical velocity profiles (i.e. deviations between local velocity and depth-averaged velocity). In hydrodynamic systems where secondary currents and stratification are insignificant, this final contribution is generally small compared to turbulent momentum flux and is often neglected (see Reference 5). The effective stresses may therefore be approximated by the turbulent stress terms only, and Boussinesq's eddy viscosity concept invoked to give

$$T_{xx}=2\rho\nu_t\frac{\partial U}{\partial x}, \qquad T_{xy}=\rho\nu_t\left[\frac{\partial U}{\partial y}+\frac{\partial V}{\partial x}\right] \quad \text{and} \quad T_{yy}=2\rho\nu_t\frac{\partial V}{\partial y}, \qquad \text{(3)}$$

where ν_t is the eddy viscosity coefficient, and is equivalent to a depth-averaged value (in order to produce the correct form of the effective stresses when integrated over depth).

In certain cases of wide rivers, shallow lakes and reservoirs where the free surface is invariant with time and nearly horizontal, a fixed-lid approximation (that is, $\partial D/\partial t$ is zero) may be used to reduce the above three equation system to two equations, with the depth-averaged stream function, ψ, and vorticity, ω, as dependent variables. It should be noted that the rigid-lid approximation filters out gravity waves, and therefore the following approach cannot be used for tidal estuaries, etc.

We define the depth-averaged stream function, ψ, from the following expressions:

$$U=\frac{1}{D}\frac{\partial\psi}{\partial y} \quad\text{and}\quad V=-\frac{1}{D}\frac{\partial\psi}{\partial x}, \tag{4}$$

which satisfy continuity. After applying the Leibnitz rule, and substituting for depth-averaged velocities, the depth-averaged vorticity may be written as

$$\omega=\frac{\partial V}{\partial x}-\frac{\partial U}{\partial y}. \tag{5}$$

The depth-averaged stream function and vorticity have essentially the same meaning as their 3D non depth-averaged counterparts. Here, ψ represents local values of the integrated depth-averaged velocity field, whereas ω, though now a 2D scalar quantity, since it acts about a vertical axis, is directly related to the rotationality of the flow at a particular point.

Substitution of equations (4) into equation (5) yields an elliptic Poisson equation for stream function:

$$\frac{\partial}{\partial x}\left[\frac{1}{D}\frac{\partial\psi}{\partial x}\right]+\frac{\partial}{\partial y}\left[\frac{1}{D}\frac{\partial\psi}{\partial y}\right]+\omega=0. \tag{6}$$

This equation indicates that the depth-averaged vorticity is effectively equal but opposite in sign to the curvature of the stream function (the sign convention is anticlockwise positive).

The depth-averaged momentum equations (2b) and (2c) are reduced to a single equation after cross-differentiation and subtraction in order to eliminate the free-surface gradients $\partial\zeta/\partial x$ and $\partial\zeta/\partial y$. After some rearrangement, the 2D depth-averaged vorticity transport equation is given by

$$\begin{aligned}&\frac{\partial\omega}{\partial t}+U\frac{\partial\omega}{\partial x}+V\frac{\partial\omega}{\partial y}+(\omega+f)\left[\frac{\partial U}{\partial x}+\frac{\partial V}{\partial y}\right]+\left[\frac{\partial}{\partial y}\left(\frac{\tau_{\mathrm{wx}}}{\rho D}\right)-\frac{\partial}{\partial x}\left(\frac{\tau_{\mathrm{wy}}}{\rho D}\right)\right]\\ &\quad-\left[\frac{\partial}{\partial y}\left(\frac{\tau_{\mathrm{bx}}}{\rho D}\right)-\frac{\partial}{\partial x}\left(\frac{\tau_{\mathrm{by}}}{\rho D}\right)\right]-\frac{1}{\rho}\frac{\partial}{\partial y}\left[\frac{1}{D}\left(\frac{\partial(DT_{xx})}{\partial x}+\frac{\partial(DT_{xy})}{\partial y}\right)\right]-\frac{1}{\rho}\frac{\partial}{\partial x}\left[\frac{1}{D}\left(\frac{\partial(DT_{xy})}{\partial x}+\frac{\partial(DT_{yy})}{\partial y}\right)\right]=0.\end{aligned} \tag{7}$$

This equation is identical in form to that presented by Kuipers and Vreugdenhil,[3] except for their use of the opposite sign convention for vorticity. The depth-averaged vorticity transport equation governs the transport, generation and dissipation of vorticity. As discussed by Kuipers and Vreugdenhil, the advection of vorticity by the mean flow is governed by the second and third terms. The fourth and fifth produce vorticity from the divergence or convergence of the mean flow, and by the action of wind stresses. Dissipation due to the bottom shear stress is given in the sixth term. Finally, the remaining two terms may be regarded as net moments of the stresses T_{xx}, T_{xy} and T_{yy} relative to a vertical axis and can generate vorticity in either direction.

The above stream function equation (6) and vorticity-transport equation (7) are converted into curvilinear form using Jacobian transformations described by Johnson and Thompson.[14] For brevity, the subscripts ξ and η will be used to denote partial derivatives in the following equations.

The curvilinear mesh is generated as the solution of

$$\alpha x_{\xi\xi}-2\beta x_{\xi\eta}+\gamma x_{\eta\eta}+J^2(Px_\xi+Qx_\eta)=0 \tag{8a}$$

and

$$\alpha y_{\xi\xi}-2\beta y_{\xi\eta}+\gamma y_{\eta\eta}+J^2(Py_\xi+Qy_\eta)=0, \tag{8b}$$

where

$$\alpha=x_\eta^2+y_\eta^2, \qquad \beta=x_\xi x_\eta+y_\xi y_\eta, \qquad \gamma=x_\xi^2+y_\xi^2,$$

and J is the Jacobian of the transformation given by

$$J=x_\xi y_\eta-x_\eta y_\xi\,.$$

In equations (8), the functions P and Q control the co-ordinate line spacing, allowing the generation of nearly square curvilinear meshes. Since the computations are to be carried out in the transformed rectangular plane, the governing equations must also be transformed. For example, the Cartesian depth-averaged velocities, U and V, are given in (ξ,η) form as

$$U=\frac{1}{DJ}(x_\xi\psi_\eta-x_\eta\psi_\xi) \quad \text{and} \quad V=\frac{1}{DJ}(y_\xi\psi_\eta-y_\eta\psi_\xi) \tag{9}$$

and the transformed depth-averaged vorticity is obtained as

$$\omega=\frac{1}{J}(x_\eta U_\xi-x_\xi U_\eta+y_\eta V_\xi-y_\xi V_\eta). \tag{10}$$

After rewriting equation (6) in the expanded form in order to facilitate straightforward transformation of second derivative terms, the transformed depth-averaged stream function equation may be obtained as follows:

$$\alpha\psi_{\xi\xi}-2\beta\psi_{\xi\eta}+\gamma\psi_{\eta\eta}+(\sigma+\sigma_D)\psi_\eta+(\tau+\tau_D)\psi_\xi+\omega DJ^2=0, \tag{11}$$

where α, β, γ and J have been defined previously, and σ, σ_D, τ and τ_D are defined in the appendix.

In a similar manner, the transformed depth-averaged vorticity transport equation is given by

$$\begin{aligned}
&\frac{\partial\omega}{\partial t}+\frac{1}{DJ}(\omega_\xi\psi_\eta-\omega_\eta\psi_\xi)+\frac{(\omega+f)}{D^2J}(\psi_\xi D_\eta-\psi_\eta D_\xi)\\
&\quad+\frac{1}{\rho DJ}\left[x_\xi\frac{\partial\tau_x}{\partial\eta}-x_\eta\frac{\partial\tau_x}{\partial\xi}-y_\eta\frac{\partial\tau_y}{\partial\xi}+y_\xi\frac{\partial\tau_y}{\partial\eta}+\frac{D_\xi}{D}(\tau_x x_\eta+\tau_y y_\eta)-\frac{D_\eta}{D}(\tau_x x_\xi+\tau_y y_\xi)\right]\\
&\quad+\frac{1}{\rho J^2}\left[-A\frac{\partial^2T_{xx}}{\partial\xi^2}+B\frac{\partial^2T_{xx}}{\partial\xi\partial\eta}-\Gamma\frac{\partial^2T_{xx}}{\partial\eta^2}-(T+T_{\mathrm{D}x})\frac{\partial T_{xx}}{\partial\xi}-(S+S_{\mathrm{D}x})\frac{\partial T_{xx}}{\partial\eta}-\kappa T_{xx}\right]\\
&\quad+\frac{1}{\rho J^2}\left[\alpha_m\frac{\partial^2T_{xy}}{\partial\xi^2}-2\beta_m\frac{\partial^2T_{xy}}{\partial\xi\partial\eta}+\gamma_m\frac{\partial^2T_{xy}}{\partial\eta^2}+(\tau_m+\tau_{\mathrm{D}m})\frac{\partial T_{xy}}{\partial\xi}+(\sigma_m+\sigma_{\mathrm{D}m})\frac{\partial T_{xy}}{\partial\eta}+\lambda T_{xy}\right]\\
&\quad+\frac{1}{\rho J^2}\left[A\frac{\partial^2T_{yy}}{\partial\xi^2}-B\frac{\partial^2T_{yy}}{\partial\xi\partial\eta}+\Gamma\frac{\partial^2T_{yy}}{\partial\eta^2}+(T+T_{\mathrm{D}y})\frac{\partial T_{yy}}{\partial\xi}+(S+S_{\mathrm{D}y})\frac{\partial T_{yy}}{\partial\eta}+\kappa T_{yy}\right]=0.
\end{aligned} \tag{12}$$

Details of the coefficients A, B, Γ, S, $S_{\mathrm{D}x}$, T, $T_{\mathrm{D}x}$, etc., are given in the appendix. The terms τ_x and τ_y, which appear in the third and fourth brackets, are the combination of wind and bed stresses in the x- and y-directions, respectively, i.e.

$$\tau_x=\tau_{\mathrm{w}x}-\tau_{\mathrm{b}x} \quad \text{and} \quad \tau_y=\tau_{\mathrm{w}y}-\tau_{\mathrm{b}y}\,.$$

Equations (11) and (12) form a pair of coupled equations relating stream function and vorticity; they are considerably more complicated than their counterparts in Cartesian co-ordinates, but are more straightforward to discretize.

The depth-averaged effective stresses are transformed to give

$$T_{xx}=\frac{2\rho\nu_t}{J}[y_\eta U_\xi-y_\xi U_\eta],$$

$$T_{xy}=\frac{\rho\nu_t}{J}[x_\xi U_\eta-x_\eta U_\xi+y_\eta V_\xi-y_\xi V_\eta],$$

$$T_{yy}=\frac{2\rho\nu_t}{J}[x_\xi V_\eta-x_\eta V_\xi], \tag{13}$$

where ν_t is the eddy viscosity coefficient. As Kaar[29] showed, significantly longer expressions for the effective stresses may be derived in terms of the stream function.

NUMERICAL SOLUTION

The grid consisted of a non-staggered square mesh of spacing $\Delta\xi=\Delta\eta=1$ in the transformed plane where all flow variables (ψ, ω, etc.) and metric parameters (J, α, β, etc.) are stored at each node. Mesh indices, $i=1,\ldots,M$ and $j=1,\ldots,N$, are defined such that $\xi=i$ and $\eta=j$. In order to generate the grid, equations (8a) and (8b) were discretized using central differences and solved iteratively using successive over-relaxation for prescribed boundary values of x and y until the normalized error was less than 10^{-8}.

The transformed depth-averaged stream function equation (11) was also discretized using second-order accurate central differences to give

$$\begin{aligned}\psi_{i,j}=\frac{1}{2(\alpha_{i,j}+\gamma_{i,j})}\Big\{&\omega_{i,j}D_{i,j}J_{i,j}^2+\alpha_{i,j}(\psi_{i+1,j}+\psi_{i-1,j})\\&-\frac{\beta_{i,j}}{2}(\psi_{i+1,j+1}-\psi_{i+1,j-1}+\psi_{i-1,j-1}-\psi_{i-1,j+1})+\gamma_{i,j}(\psi_{i,j+1}+\psi_{i,j-1})\\&+\tfrac{1}{2}(\sigma_{i,j}+\sigma_{D_{i,j}})(\psi_{i,j+1}-\psi_{i,j-1})+\tfrac{1}{2}(\tau_{i,j}+\tau_{D_{i,j}})(\psi_{i+1,j}-\psi_{i-1,j})\Big\}\end{aligned} \tag{14}$$

and solved using successive over-relaxation.

An ADI procedure was used to update the depth-averaged vorticity values over two half time steps. At the nth time increment, the time is defined to be $t=n\,\Delta t$, where Δt is the time step. In the first half time step, from time $t=n\,\Delta t$ to $t=(n+\frac{1}{2})\Delta t$, the depth-averaged vorticity transport equation is released in the ξ-direction while holding the η-derivatives fixed, discretized using forward differences in time and central differences in space (except for the advection terms, $\omega_\xi\psi_\eta-\omega_\eta\psi_\xi$, which are treated using the first-order donor cell method), and rearranged to give

$$-a_i\,\omega_{i-1/2,j}^{n+1/2}+b_i\,\omega_{i,j}^{n+1/2}-c_i\,\omega_{i+1/2,j}^{n+1/2}=k_i\,, \tag{15}$$

where

$$a_i=\frac{1}{D_{i,j}^n J_{i,j}}\psi_\eta|_{i-1/2,j}^n,\qquad b_i=\frac{2}{\Delta t},\qquad c_i=-\frac{1}{D_{i,j}^n J_{i,j}}\psi_\eta|_{i+1/2,j}^n$$

and

$$k_i = -\frac{\omega^{\eta}_{i,j-1/2}}{D^n_{i,j}J_{i,j}}\,\psi_\xi\big|^{n+1/2}_{i,j-1/2} + \frac{2}{\Delta t}\,\omega^n_{i,j} + \frac{\omega^{\eta}_{i,j+1/2}}{D^n_{i,j}J_{i,j}}\,\psi_\xi\big|^{n+1/2}_{i,j+1/2}$$
$$-\frac{(\omega^n_{i,j}+f)}{D^n_{i,j}D^n_{i,j}J_{i,j}}\left(\psi_\xi\big|^{n+1/2}_{i,j}\,D_\eta\big|^n_{i,j} - \psi_\eta\big|^n_{i,j}\,D_\xi\big|^{n+1/2}_{i,j}\right) - R1_{i,j} - R2_{i,j}$$
$$-R3_{i,j} - R4_{i,j} - R5_{i,j} - R6_{i,j} - R7_{i,j} - R8_{i,j}$$

in which

$$R1_{i,j} = \frac{1}{\rho D^n_{i,j}J_{i,j}}\left[x_\xi\frac{\partial\tau_x}{\partial\eta}\bigg|^n_{i,j} - x_\eta\frac{\partial\tau_x}{\partial\xi}\bigg|^{n+1/2}_{i,j} - y_\eta\frac{\partial\tau_y}{\partial\xi}\bigg|^{n+1/2}_{i,j} + y_\xi\frac{\partial\tau_y}{\partial\eta}\bigg|^n_{i,j}\right],$$

$$R2_{i,j} = \frac{1}{\rho D^n_{i,j}J_{i,j}}\left[\frac{D_\xi}{D}(\tau_x x_\eta + \tau_y y_\eta)\bigg|^{n+1/2}_{i,j} - \frac{D_\eta}{D}(\tau_x x_\xi + \tau_y y_\xi)\bigg|^n_{i,j}\right],$$

$$R3_{i,j} = \frac{1}{\rho J^2_{i,j}}\left[-A\frac{\partial^2 T_{xx}}{\partial\xi^2}\bigg|^{n+1/2}_{i,j} + B\frac{\partial^2 T_{xx}}{\partial\xi\partial\eta}\bigg|^{n+1/2}_{i,j} - \Gamma\frac{\partial^2 T_{xx}}{\partial\eta^2}\bigg|^n_{i,j}\right],$$

$$R4_{i,j} = \frac{1}{\rho J^2_{i,j}}\left[-(T+T_{\mathrm{D}x})\frac{\partial T_{xx}}{\partial\xi}\bigg|^{n+1/2}_{i,j} - (S+S_{\mathrm{D}x})\frac{\partial T_{xx}}{\partial\eta}\bigg|^n_{i,j} - \kappa T_{xx}\bigg|^n_{i,j}\right],$$

$$R5_{i,j} = \frac{1}{\rho J^2_{i,j}}\left[\alpha_m\frac{\partial^2 T_{xy}}{\partial\xi^2}\bigg|^{n+1/2}_{i,j} - 2\beta_m\frac{\partial^2 T_{xy}}{\partial\xi\partial\eta}\bigg|^{n+1/2}_{i,j} + \gamma_m\frac{\partial^2 T_{xy}}{\partial\eta^2}\bigg|^n_{i,j}\right],$$

$$R6_{i,j} = \frac{1}{\rho J^2_{i,j}}\left[(\tau_m + \tau_{\mathrm{D}m})\frac{\partial T_{xy}}{\partial\xi}\bigg|^{n+1/2}_{i,j} + (\sigma_m + \sigma_{\mathrm{D}m})\frac{\partial T_{xy}}{\partial\eta}\bigg|^n_{i,j} + \lambda T_{xy}\bigg|^n_{i,j}\right],$$

$$R7_{i,j} = \frac{1}{\rho J^2_{i,j}}\left[A\frac{\partial^2 T_{yy}}{\partial\xi^2}\bigg|^{n+1/2}_{i,j} - B\frac{\partial^2 T_{yy}}{\partial\xi\partial\eta}\bigg|^{n+1/2}_{i,j} + \Gamma\frac{\partial^2 T_{yy}}{\partial\eta^2}\bigg|^n_{i,j}\right],$$

and

$$R8_{i,j} = \frac{1}{\rho J^2_{i,j}}\left[(T+T_{\mathrm{D}y})\frac{\partial T_{yy}}{\partial\xi}\bigg|^{n+1/2}_{i,j} + (S+S_{\mathrm{D}y})\frac{\partial T_{yy}}{\partial\eta}\bigg|^n_{i,j} + \kappa\,T_{yy}\bigg|^n_{i,j}\right].$$

Equation (15) is applied at each grid point along a given j-line to give a set of $M-2$ linear simultaneous equations. These are expressed in tridiagonal matrix form and solved recursively. In the second half time step, from $t=(n+\frac{1}{2})\Delta t$ to $t=(n+1)\Delta t$, the discretization procedure involves releasing derivatives in the η-direction while keeping the ξ-derivatives fixed, giving

$$-a_j\,\omega^{n+1}_{i,j-1/2} + b_j\,\omega^{n+1}_{i,j} - c_j\,\omega^{n+1}_{i,j+1/2} = k_j\,, \tag{16}$$

where

$$a_j = -\frac{1}{D^{n+1/2}_{i,j}\,J_{i,j}}\,\psi_\xi\big|^{n+1/2}_{i,j-1/2}, \qquad b_j = \frac{2}{\Delta t}, \qquad c_j = \frac{1}{D^{n+1/2}_{i,j}\,J_{i,j}}\,\psi_\xi\big|^{n+1/2}_{i,j+1/2}$$

and

$$k_j = \frac{\omega^{n+1/2}_{i-1/2,j}}{D^{n+1/2}_{i,j}\,J_{i,j}}\,\psi_\eta\big|^{n+1}_{i-1/2,j} + \frac{2}{\Delta t}\,\omega^{n+1/2}_{i,j} - \frac{\omega^{n+1/2}_{i+1/2,j}}{D^{n+1/2}_{i,j}\,J_{i,j}}\,\psi_\eta\big|^{n+1}_{i+1/2,j}$$
$$-\frac{(\omega^{n+1/2}_{i,j}+f)}{D^{n+1/2}_{i,j}\,D^{n+1/2}_{i,j}\,J_{i,j}}\left(\psi_\xi\big|^{n+1/2}_{i,j}\,D_\eta\big|^{n+1}_{i,j} - \psi_\eta\big|^{n+1}_{i,j}\,D_\xi\big|^{n+1/2}_{i,j}\right) - R1_{i,j} - R2_{i,j}$$
$$-R3_{i,j} - R4_{i,j} - R5_{i,j} - R6_{i,j} - R7_{i,j} - R8_{i,j}$$

in which the terms $R1_{i,j}$ to $R8_{i,j}$ are the same as for the first release, except that the superscripts n become $n+1$.

In each half time step, the spatial discretization error is of the order of $(\Delta\xi^2, \Delta\eta^2)$. The ADI method may also give the time dependency with an error of the order of (Δt^2) provided the terms at $n+\frac{1}{2}$ in the first release, and $n+1$ in the second release, are evaluated correctly. It should be noted that true second-order time accuracy may only be achieved by an iterative procedure coupling the solution of the depth-averaged stream function and vorticity transport equations. For the results presented in this paper, the right-hand terms in equations (15) and (16) were lagged in order to cut down on the computational costs; this increased the error in temporal accuracy to first order, but had marginal effect for flows which tend to steady state (considered later).

As mentioned above, all spatial derivatives in the above equations, except for the advection terms given by $\omega_\xi\psi_\eta-\omega_\eta\psi_\xi$, were discretized using central differences. In order to achieve stability, but without undue artificial diffusion, three approaches were adopted for the advection terms; namely, the donor cell method, second-order upwind differencing and Stelling's[19] weighted averaging scheme of $\frac{2}{3}$ central plus $\frac{1}{3}$ upwind differencing. Obviously, each scheme affects the coefficients a, b, c and k. For example, in the donor cell method (which turned out to be the most successful for the cases considered here and is used to produce equations (15) and (16) above), the advection terms are discretized over one cell length giving

$$\omega_\xi\psi_\eta-\omega_\eta\psi_\xi=\psi_\eta\omega\,|_{i+1/2,j}-\psi_\eta\omega\,|_{i-1/2,j}-\psi_\xi\omega\,|_{i,j+1/2}+\psi_\xi\omega\,|_{i,j-1/2}\;,$$

where

$$\psi_\eta\,|_{i+1/2,j}=\tfrac{1}{2}(\psi_\eta\,|_{i+1,j}+\psi_\eta\,|_{i,j})\;,\text{ etc.}$$

and

$$\begin{aligned}
&\omega_{i+1/2,j}=\omega_{i,j} && \text{if } \psi_\eta\,|_{i+1/2,j}>0,\\
&\omega_{i+1/2,j}=\omega_{i+1,j} && \text{if } \psi_\eta\,|_{i+1/2,j}<0,\\
&\omega_{i-1/2,j}=\omega_{i-1,j} && \text{if } \psi_\eta\,|_{i-1/2,j}>0,\\
&\omega_{i-1/2,j}=\omega_{i,j} && \text{if } \psi_\eta\,|_{i-1/2,j}<0.
\end{aligned}$$

Similar expressions are obtained for $\omega_{i,j+1/2}$ and $\omega_{i,j-1/2}$ depending on the sign of ψ_ξ (and hence the appropriate contravariant velocity component). In operation, the k_i and k_j coefficients are easily computed, but care needs to be taken with the a, b and c coefficients which depend on the sign of ψ_η in the ξ-direction release and ψ_ξ in the η-direction release. Although the donor cell method is strictly only first-order accurate, it possesses the transportive property and may approach second-order accuracy if the vorticity varies slowly in space. Further details of the implementation of the donor cell method, the second-order upwind differencing and weighted averaging scheme are given by Kaar.[29]

In order to drive the flow, the stream function was set to zero at one wall boundary and equal to $U_\text{I}Db_\text{I}$ at the opposite wall (where U_I is the inlet flow velocity, D the depth and b_I the inlet width). No-slip wall vorticity conditions are derived by simplifying the depth-averaged stream function equation (11), depending on which ψ-derivatives are zero, and applying Taylor series up to terms of order $(\Delta\eta^2)$ to give expressions such as

$$\omega_{i,j}=\frac{2\gamma_{i,j}}{D_{i,j}J_{i,j}^2}(\psi_{i,j}-\psi_{i,j+1})\;, \tag{17}$$

which applies to a lower wall located at $j=1$, say. Vorticity values at convex corner points were determined by treating the point as if it were at a $\xi=$constant wall during the ξ-release, and at an $\eta=$constant wall during the η-release. For the backward-facing step, the vorticity at the concave corner is zero by definition. For the circular reservoir, the concave corner points correspond to inflexion points in the physical domain and so vorticity values were obtained by extrapolation. It should be noted that the above no-slip condition does not cater properly for a turbulent boundary layer; in such a case, either a more realistic condition related to a suitable wall law, or else a partial-slip condition should be applied.

Parallel flow was assumed at open (inflow/outflow) boundaries. For example, flow normal to lines of constant ξ is determined by $\partial f/\partial \mathbf{n}(\xi)=\mathbf{n}(\xi)\cdot\nabla f=0$, where $\mathbf{n}(\xi)$ is the unit vector normal to ξ, and f represents ψ or ω. This may be expressed as $\alpha f_\xi=\beta f_\eta$ and discretized using second-order differences to give

$$f_{i,j}=\frac{1}{3}\left[4f_{i+1,j}-f_{i+2,j}-\frac{\beta_{i,j}}{\alpha_{i,j}}(f_{i,j+1}-f_{i,j-1})\right] \tag{18}$$

for a typical (left hand, $i=1$ say) flow boundary.

Interior values of the depth-averaged effective stresses given by equation (13) were determined from their central difference discretizations. At boundaries, the effective stresses were calculated using second-order forward and backward differences. Very high velocity and vorticity gradients occur near the boundary, and five-point Lagrange interpolation was applied to calculate effective stresses one point out from the boundary giving, e.g.,

$$T_{xx_{i+1,j}}=\tfrac{1}{4}[T_{xx_{i,j}}+6T_{xx_{i+2,j}}-4T_{xx_{i+3,j}}+T_{xx_{i+4,j}}] \tag{9}$$

at a point immediately adjacent to a left-hand boundary.

The potential flow solution was used as a starting condition for the flow computations. Everywhere ω was set to zero, and the initial ω-field determined by solving equation (11). The computations then proceeded in a cyclic time-stepping manner, updating vorticity, stream function and effective stresses until steady state was judged to have occurred.

RESULTS

Two validation tests are considered here. First, the (ψ,ω) computer model is used to simulate laminar flow past a backward-facing step. In this case, the recirculating flow is dominated by the non-linear advection terms in the vorticity-transport equation and it is possible to identify the level of artificial viscosity generated by the scheme. In the second case, jet-forced flow in a circular reservoir is simulated at low Reynolds numbers. This geometry provides a severe test of the curvilinear system, because the perimeter is everywhere curved with vertical walls, and the flow is separated. The results are compared with analytical solutions, alternative numerical simulations and experimental data.

All computations took place on a 16 MHz IBM PS/2 Model 80 microcomputer containing 2 Mb RAM without vector facility. The microcomputer architecture consisted of an 80386DX processor with an 80387 mathematics co-processor. The computer program was written in Fortran 77 using double precision.

Laminar flow past a backward facing step

Figure 2 illustrates laminar flow past a backward-facing step, which is characterized by separation at the step followed by a recirculation zone. A measure of computational accuracy is given by the prediction of the reattachment point, defined by a vorticity sign change. The zones of

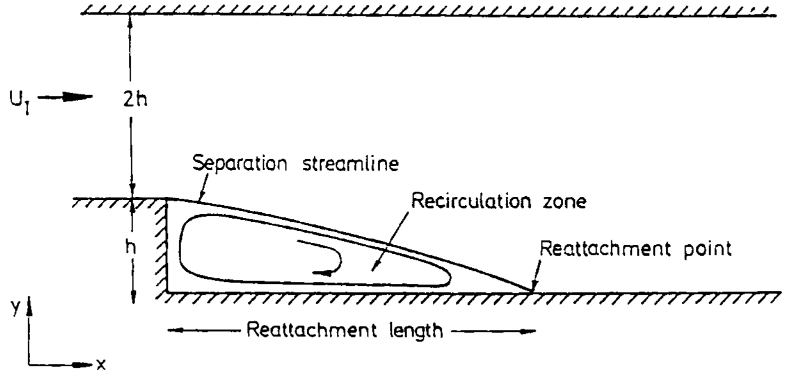

Figure 2. Flow past a backward facing step

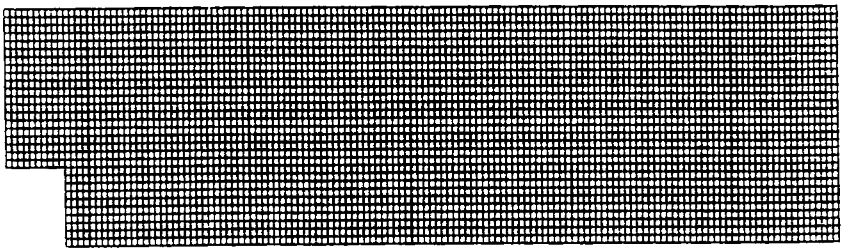

Figure 3. Computational grid

recirculation reduce in length when artificial viscosity (arising from poorly discretized advection terms) overwhelms the correct effective viscosity of the flow. Provided the flow is laminar, the reattachment length increases with Reynolds number; typical references include the work of O'Leary and Mueller,[30] Denham and Patrick,[31] Atkins *et al.*[32] and Hackman *et al.*[33]

The computational geometry consists of a rectangular channel of length 14 m, inlet width 2 m and step dimension of 1 m. The upstream boundary is one step dimension, *h*, in front of the expansion, whereas the outflow boundary is more than 5 *h* beyond the reattachment point, in accordance with advice given by Hackman *et al.*[33] To check grid resolution, two meshes are used; one a coarse grid with 71 × 16 nodes, where $\Delta x = \Delta y = 0{\cdot}2$ m, the other a fine grid (shown in Figure 3) with 141 × 31 nodes, where $\Delta x = \Delta y = 0{\cdot}1$ m. Stream function values of 0 and 1 are assigned to the upper and lower walls, respectively, and the depth set to 1 m, equivalent to an average inlet velocity of 0·5 m/s. Wind and bed shear stresses are zero. Time steps are determined from the Courant condition to be $\Delta t = 0{\cdot}4$ and 0·2 s for the coarse and fine meshes, respectively. Results are presented for inlet Reynolds numbers between 46 and 229, corresponding to the experiments of Denham and Patrick.[31] Here, the inlet Reynolds number, Re_I, is defined by

$$Re_I = \frac{U_I h}{\nu} \tag{20}$$

where U_I is the average inlet velocity, *h* is the step dimension and ν is the kinematic viscosity coefficient.

Figure 4 gives stream function, vorticity and velocity plots of the steady-state flow pattern using donor cell differencing, at $Re_l = 229$. As would be expected, the main flow pattern consists of a primary recirculation zone immediately behind the backward-facing step, adjacent to a fast throughflow. Vorticity contours have high magnitude and steep gradients at the lower wall immediately preceding the step and on the upper wall near the inlet. From these regions, loops of vorticity spread out into the field. The variation of vorticity on the upper wall, reflected in the

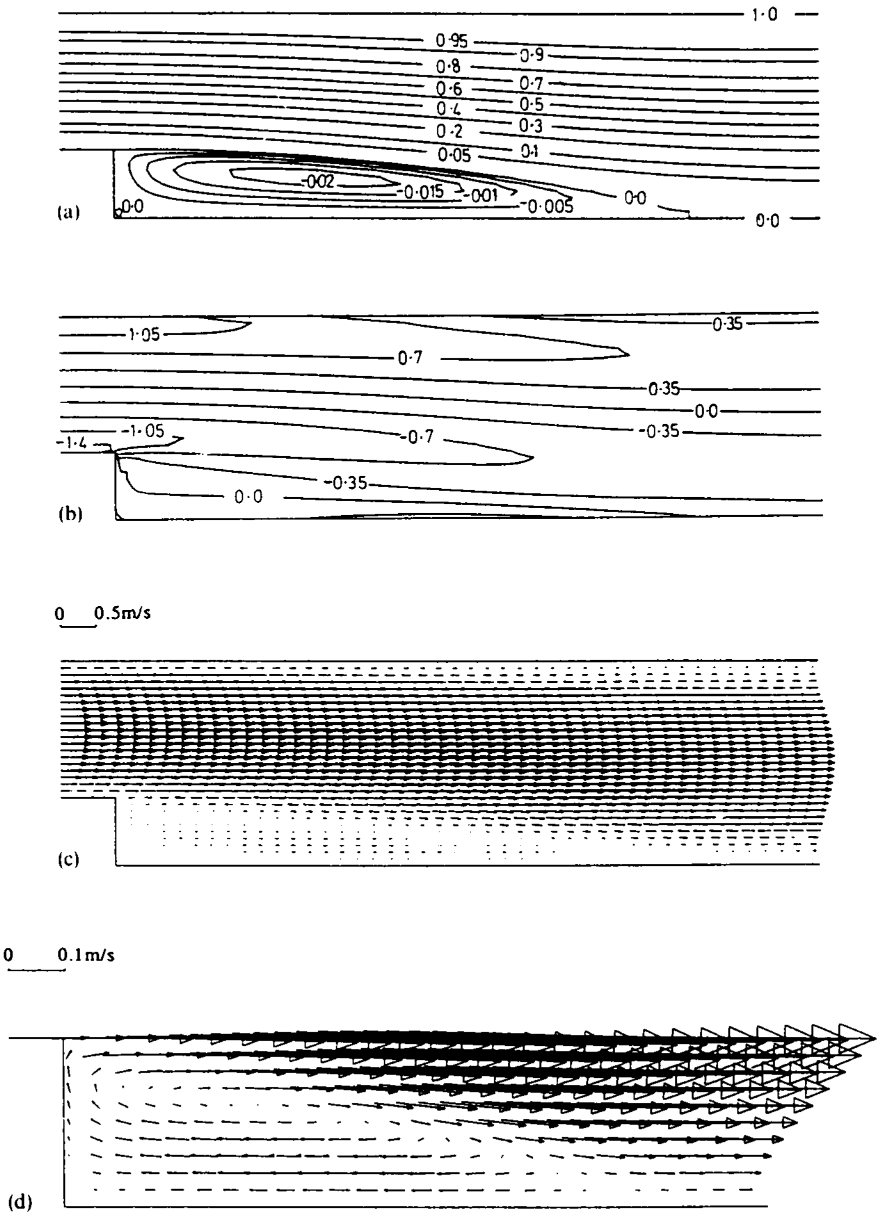

Figure 4. Flow pattern for $Re_l = 229$ (donor cell method): (a) stream function contours; (b) vorticity contours; (c) velocity vectors; (d) detail of structure in gyre

velocity plot which shows a slowing down of fluid in this region, points to possible recirculation in this location. A small secondary gyre occurs in the lower left-hand concave corner caused by the sudden change in geometry.

The effect of grid resolution on reattachment length for predictions using the donor cell method is illustrated in Figure 5. In general, the fine-grid simulations show good agreement with experimental and numerical data obtained by O'Leary and Mueller[30] and Denham and Patrick.[31] For the coarse grid, recirculation is underpredicted at Reynolds numbers greater than about 100, thus indicating the presence of artificial viscosity caused by truncation errors whose magnitude increases with Reynolds number. The finer mesh consistently produces longer recirculation lengths than Denham and Patrick's experimental data, even at higher Reynolds numbers. This may be due to asymmetry in the experimental inflow conditions (discussed later). Similar numerical studies by Hackman *et al.*[33] also gave longer recirculation lengths than measured experimentally. It should be noted that further grid refinement was not possible in this study due to microcomputer memory limitations.

The reattachment length was used to compare the effectiveness of the three discretization schemes for the non-linear advection terms in the depth-averaged vorticity transport equation. For $Re_I < 125$, all three methods produced nearly identical results which is to be expected because the level of artificial viscosity was relatively small. Weighted second-order and donor cell differencing continued to give very similar reattachment lengths throughout the range of Reynolds numbers considered. This may be because the donor cell method took into account values at half grid spacings on either side of each mesh point and approached second-order accuracy where the spatial variation of vorticity was small. For $Re_I > 125$, pure second-order differencing produced smaller recirculation zones than either weighted differencing or the donor

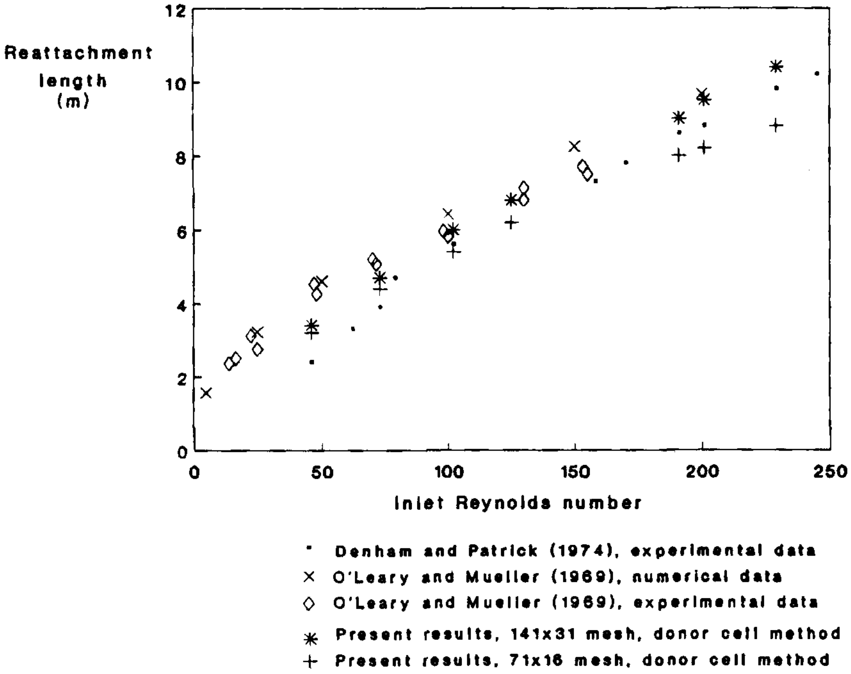

Figure 5 Dependence of reattachment length on inlet Reynolds number

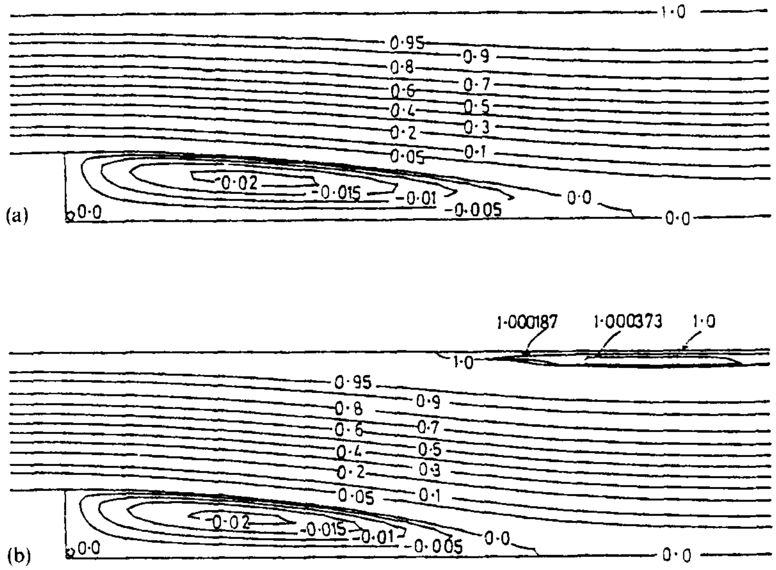

Figure 6. Stream function contours for $Re_1=229$; (a) Stelling's[19] weighted differencing scheme; (b) second-order upwind differencing scheme

cell method, which indicates that artificial viscosity is higher in the pure second-order scheme. Figure 6(a) shows stream function contours obtained using Stelling's[19] weighted averaging scheme for the advection terms. No upper recirculation may be discerned. However, for the pure second-order upwind scheme, the streamline bounding the smaller primary gyre has a steeper gradient near the reattachment point and separation occurs at the upper wall in Figure 6(b). It should be noted that vorticity is very nearly zero in the region of the upper separation zone; this may make stream function values sensitive to numerical round-off errors which could also play a part in disturbing the flow pattern.

Figure 7 illustrates velocity profiles along the channel for $Re_1=73$. The predicted velocity profile across the inlet is very similar to the measured values. At higher Reynolds numbers however, the measured inlet profiles became increasingly skewed towards the step (which Denham and Patrick attributed to asymmetry of the inlet), whereas predicted values retained their parabolic shape. This may explain the difference between experimental and predicted reattachment lengths. Moreover, Atkins *et al.*[32] have demonstrated that rather longer recirculation lengths are obtained when parabolic, instead of measured, profiles are used.

Jet-forced flow in a circular reservoir

The second validation test concerns jet-forced flow in a flat-bottomed circular reservoir at low Reynolds numbers. Two geometries are considered herein; one where inlet and outlet channels are diametrically opposite, the other where they are asymmetric. In this case, we define the inlet Reynolds number to be

$$Re_1=\frac{U_1 b_1}{2\nu}, \tag{21}$$

where U_1 is the mean inlet velocity, b_1 is the inlet width and ν is the kinematic viscosity coefficient.

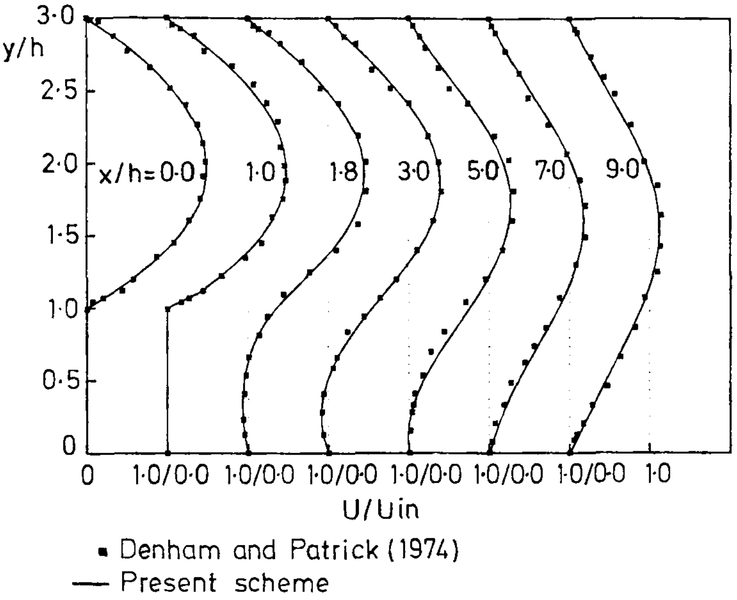

Figure 7. Velocity profiles along channel for $Re_{\mathrm{I}}=73$

Results using Dennis'[34] geometry. The first geometry considered is identical to that used by Dennis,[34] Barber[35] and Borthwick and Barber[36, 23] where a single inflow and a single outflow are positioned directly opposite each other. Dennis[34] solved the two-dimensional Navier–Stokes equations in polar form by substituting Fourier series for the stream function and vorticity. He obtained an exact analytical solution for Stokes flow (where $Re_{\mathrm{I}}=0$). For non-zero Reynolds numbers, Dennis used a numerical technique to solve the truncated Fourier series and presented results for inlet Reynolds numbers of 2, 5 and 10. He found that no recirculation occurred for $Re_{\mathrm{I}}<2$, but the flow separated at the inlet by $Re_{\mathrm{I}}=5$. Borthwick and Barber[36] repeated Dennis' simulation at $Re_{\mathrm{I}}=10$ and obtained almost exact agreement with Dennis' stream function contours, using a finite difference discretization of the 2D stream function and vorticity transport equations. To avoid artificial viscosity, the advection terms were discretized using central differences. Unlike Dennis, Borthwick and Barber presented vorticity and velocity distributions. In order to verify the depth-averaged (ψ, ω) model, flow at $Re_{\mathrm{I}}=10$ in a circular reservoir corresponding to Dennis' geometry is selected herein. This case covers the effects of large vorticity gradients as well as the influence of the non-linear terms in promoting separation. Moreover, the geometry necessitated the use of a non-orthogonal mesh. For the same reasons, Barber[35] also used this case to verify his depth-averaged (U, V, ζ) scheme.

Figure 8 illustrates the geometric layout used for the flow simulations, where inlet and outlet stems of width 0·157 m and length 0·3 m are located opposite each other. The stems are included in order to allow some boundary layer development in the passageways. The radius of the reservoir, R, is 0·75 m, the depth is 0·1 m and the mean inlet velocity, U_{I}, is 0·1 m/s, equivalent to stream function values of 0·0 and 0·001568 on the lower and upper walls, respectively. Figures 9(a) and 9(b) show the transformed (ξ, η) and physical (x, y) meshes generated using a relatively fine 61×61 grid to cover the circular basin. The circular perimeter of the physical mesh contains four points of inflexion at $\pi/4$, $3\pi/4$, $5\pi/4$ and $7\pi/4$ radians. These inflexion points correspond to the corners of the transformed (ξ, η) mesh.

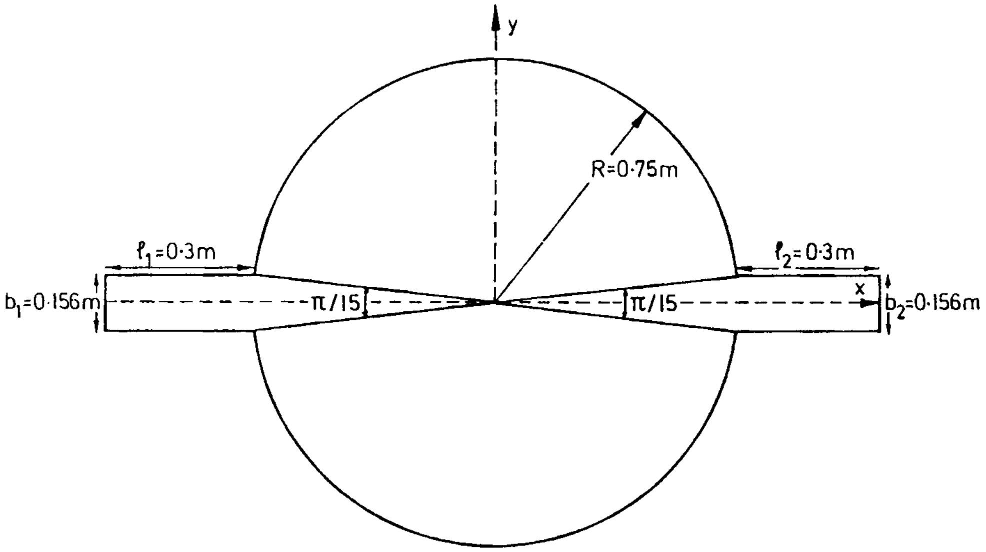

Figure 8. Reservoir definition based on Dennis'[34] geometry

The steady-state flow pattern obtained at $Re_l = 10$ is shown in Figure 10. A time step of 0·2 s was employed and steady state reached by $t = 80$ s, requiring 27 h CPU time. At such a low Reynolds number, the severe vorticity gradients in the vicinity of concave wall corner points led to grid-scale oscillations which could only be cured by the application of a spatial filter every five time steps after the separation streamlines passed close to the corner points in the transformed mesh. The spatial filter is described by Kaar[29] and consisted of weighted averages of ψ and ω at the point in question and its neighbours. Such problems were not encountered by using a coarser 31 × 31 grid where numerical diffusion acted to damp out instabilities. Even so, the results obtained using the 61 × 61 mesh are in almost exact agreement with Barber's[35] (U, V, ζ) model. The flow pattern is characterized by two symmetric zones of recirculation which are established either side of the throughflow jet which gradually fans out into the reservoir before exiting radially into the outlet stem. Stagnation regions are evident within the recirculating gyres. The throughflow contains the largest velocity components and is aligned more or less directly towards the outlet.

The stream function contours, illustrated in Figure 10(a), are scaled to lie between 0·0 and 2·0 at the lower and upper walls, respectively. Compared with Dennis'[34] 2D (ψ, ω) solution, the gyres occupy the same locations, but recirculation is stronger in the present scheme. In addition, the throughflow expands slightly less after it passes the mid-point of the reservoir, than in Dennis' solution, although agreement is exact as the flow contracts and forms its characteristic bulbous shape, before it exits through the outlet. Comparison with Borthwick and Barber's[36] Navier–Stokes simulation again shows good agreement, but strength of recirculation is noticeably overpredicted (although Borthwick and Barber obtained weaker recirculation than Dennis). The throughflow jet also shows less expansion in the later half of the basin, and reattachment of the separation streamline is nearer the outlet in the present depth-averaged (ψ, ω) scheme. Since neither Dennis[34] nor Borthwick and Barber[36] included inlet and outlet passageways at this Reynolds number, the stronger recirculation, and marginally narrower throughflow predicted herein, could be attributed to the more parabolic inlet velocity profiles, generated as the flow

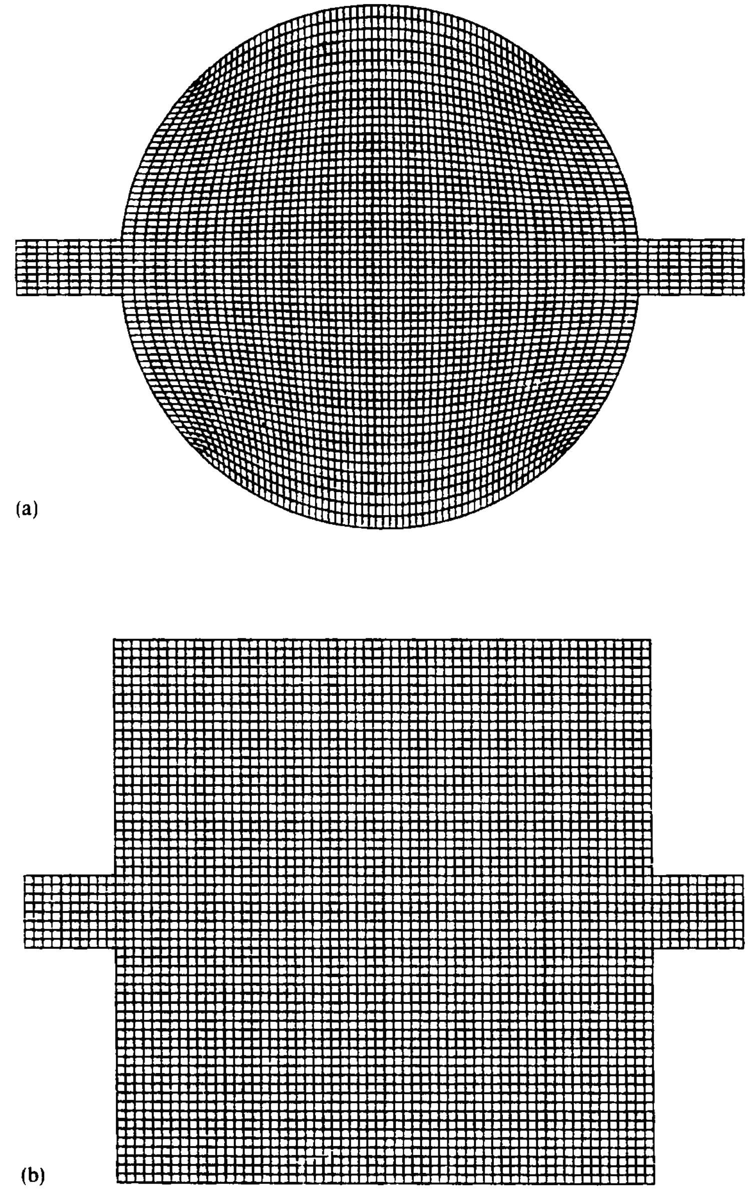

Figure 9. Reservoir meshes based on Dennis'[34] geometry: (a) physical mesh; (b) transformed mesh

travels through the inlet stem. This supports the findings of the backward-facing step validation test, where more parabolic profiles gave longer recirculation lengths. As mentioned above, the results show closest agreement to Barber's[35] boundary-fitted, primitive variable approach. Positions of the gyres are closely matched and their strength is very similar. Throughflow contours are also identical, and, although reattachment occurs at slightly different positions, this is probably caused by plotting errors due to grid resolution. The vorticity contours in Figure 10(b) indicate steep gradients of vorticity at the centre of the throughflow and close to the

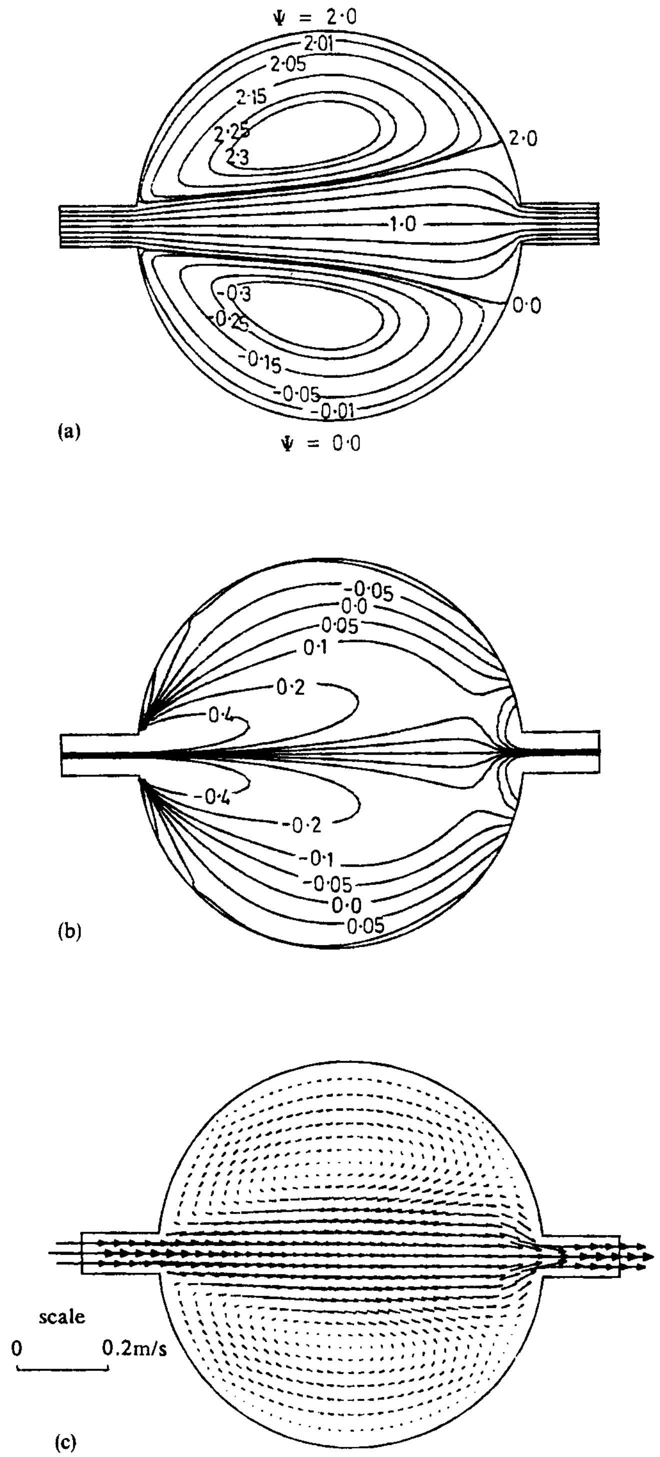

Figure 10. Predictions for $Re_1 = 10$, using a 61 × 61 mesh, Dennis' geometry: (a) stream function contours; (b) vorticity contours; (c) velocity vectors

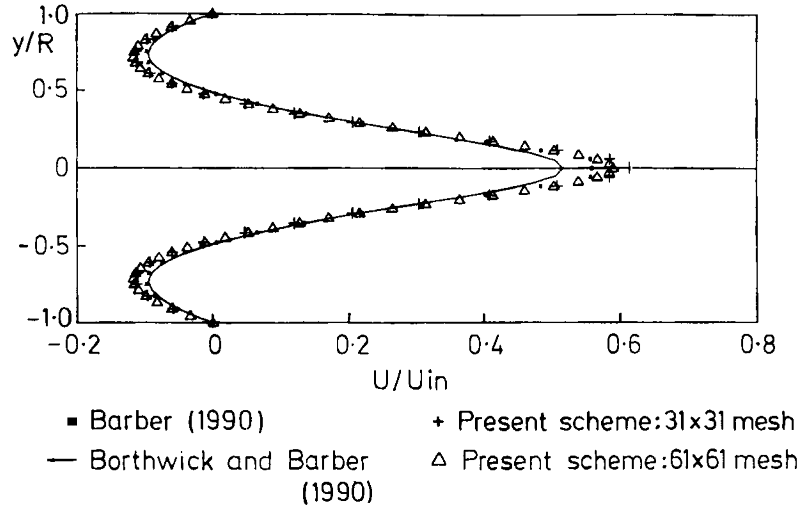

Figure 11. Velocity profiles across reservoir for $Re_I = 10$, Dennis' geometry

side walls. Loops of high vorticity are also evident at the inlet, and these loops spread out either side of the throughflow and push towards the outlet. Most of this vorticity exits through the outlet, but some is squeezed back into the basin and forms the bulging contours around the sharp corners. The velocity vectors plotted in Figure 10(c) provide a useful picture of the expansion and contraction of the jet as it enters and then leaves the reservoir, and clearly illustrate the stagnation points at the centre of each gyre.

Even so, a close examination of the velocity profiles reveals discrepancies between the models. Figure 11 illustrates profiles of the non-dimensionalized U-velocity component along the line bisecting the inlet and outlet at the mid-section of the reservoir. Results from the present scheme are plotted alongside those of Borthwick and Barber[36] and Barber.[35] Overall agreement is satisfactory, especially in the region between the throughflow and the centre of the gyres. However, the present scheme predicts higher velocities at the centre of the throughflow and in the outer portion of the gyres, near the walls. Again, this may be explained by the more parabolic inlet profiles of the present scheme. Although Barber's[35] geometry does include an inlet stem, velocity across the inlet is fixed at 0·1 m/s, whereas the present scheme is less restrictive since the stream function condition at the inlet allows the velocity to develop as part of the flow. Figure 11 indicates that little change occurs in predicted velocity patterns obtained by the coarse and fine meshes, except for a reduction in centreline velocity in the latter case.

Further results have been obtained for an inlet Reynolds number of 200. Figure 12 illustrates the flow pattern at a steady-state time of 162 s. The throughflow jet streamlines are almost exactly parallel from the inlet to the outlet where there is a final slight divergence before the flow accelerates into the outlet stem. Two vortices may be observed tightly rolled up either side of the main flow jet close to the outlet. An additional pair of slower rotating gyres are visible in the main body of the reservoir.

Results using Mills'[37] *geometry.* The second geometry, involving asymmetric inlet and outlet positions, is similar to that devised by Mills,[37] who proposed an iterative integral technique for solving 2D flows in a circle at very low inlet Reynolds numbers. Mills was able to obtain solutions for Re_I up to 7·5, but noted that numerical instability set in at $Re_I = 15$. Later, Borthwick and

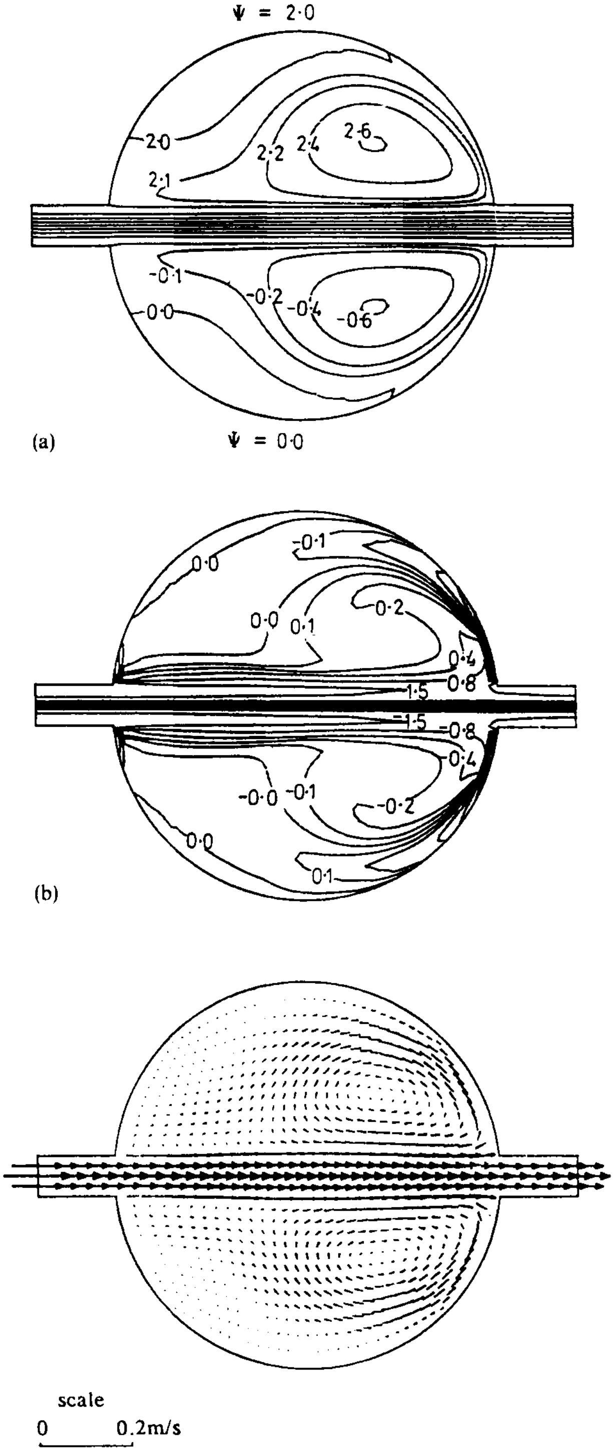

Figure 12. Predictions for $Re_1 = 200$, using a 61 × 61 mesh, Dennis' geometry: (a) stream function contours; (b) vorticity contours; (c) velocity vectors

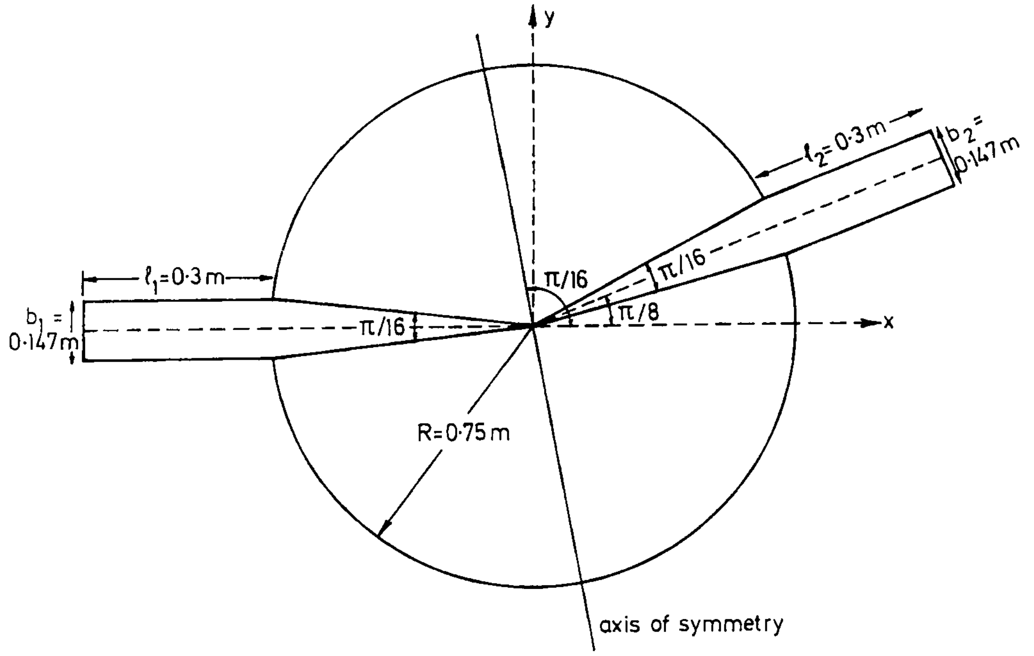

Figure 13. Reservoir definition based on Mills'[37] geometry

Barber[36] extended the cases up to a Reynolds number of 200. They found that two gyres formed for $2 < Re_I < 25$, but these increased to four by $Re_I = 100$. At $Re_I = 200$, their solution broke down due to the emergence of small vortices in the shear layers at the edges of the throughflow stream. Once these vortices reached the outlet, the steep vorticity gradients led to instability. Again, Barber[35] used some of these data to verify his depth-averaged non-orthogonal (U, V, ζ) model. In this paper, results from the non-orthogonal depth-averaged (ψ, ω) model will be compared with Borthwick and Barber's data at $Re_I = 25$, 100 and 200.

As portrayed in Figure 13, the circular reservoir contains a single inlet and a single outlet placed asymmetrically so that their centrelines are separated by an angle of $7\pi/8$ radians. The width of the inlet and outlet is 0·00147 m. All other conditions are the same as before; with the reservoir having a radius of 0·75 m, a water depth of 0·1 m and the mean inlet velocity equal to 0·1 m/s. Consequently, the lower and upper wall values of stream function are 0·0 and 0·00147, respectively. The physical mesh generated for this geometry is shown in Figure 14, where it is evident that the mesh inflexion points in the physical domain are situated so as to give a reasonably square interior mesh (i.e. the inflexion points are not quite evenly distributed around reservoir perimeter).

Figure 15 shows results obtained for an inlet Reynolds number of 25, using a 61×61 mesh with the donor cell method applied to the advective terms in the vorticity transport equation. No instabilities were experienced on the approach to steady state and so there was no requirement for spatial filtering. The scaled stream function plots show almost exact agreement with the analogous 2D Navier–Stokes model presented by Borthwick and Barber,[36] although the throughflow is a little more compressed in the present scheme. It is not possible to scale vorticity plots to match those of Borthwick and Barber's, since the authors did not specify the maximum vorticity in the field, but in Figure 15(b), the vorticity contours have been drawn at similar intervals to

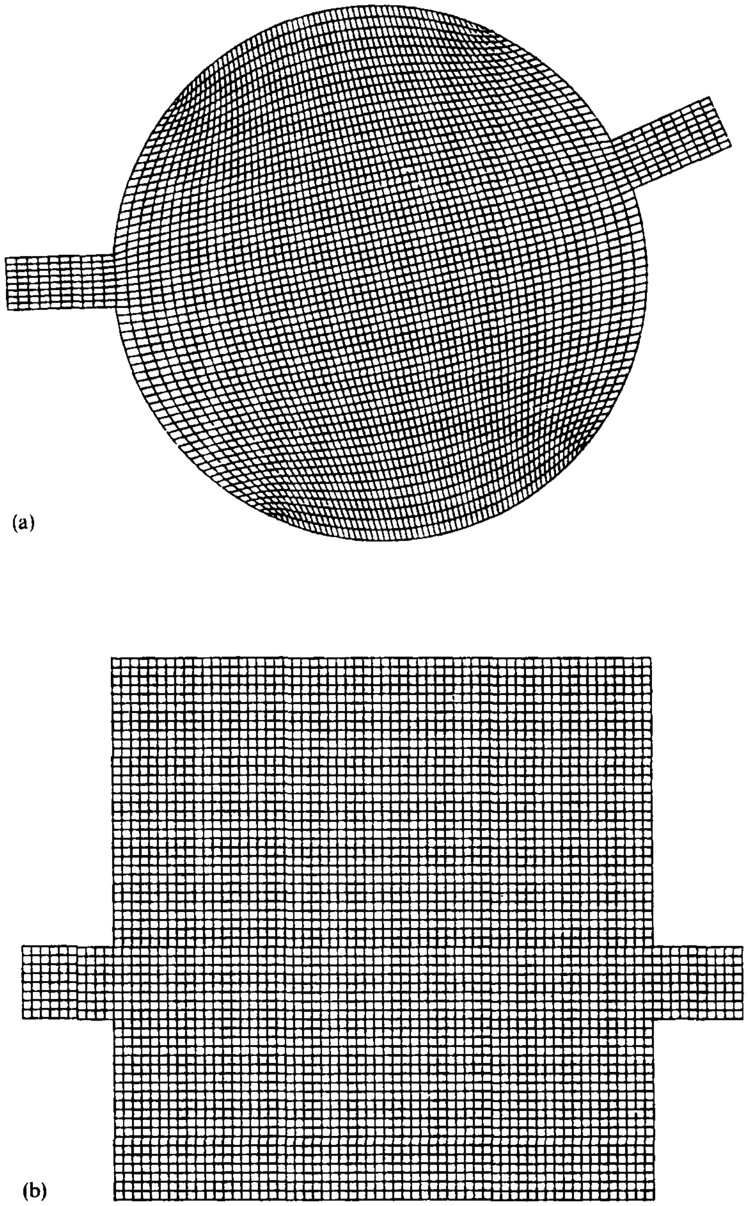

Figure 14. Reservoir meshes based on Mills'[37] geometry: (a) physical; (b) transformed

allow a qualitative comparison. Moreover, the zero vorticity lines can be compared directly, and are seen to occupy an identical position to that given by Borthwick and Barber. Agreement with Barber's[35] depth-averaged (U, V, ζ) boundary-fitted scheme is also good, although Barber predicts weaker recirculation in the lower gyre. Figure 16 shows the non-dimensionalized velocity profile across the reservoir. Here, the component of U-velocity normal to the axis of symmetry of the reservoir is plotted against radial distance from the centre along this line of symmetry. That is, Figure 16 is a non-dimensionalized plot of $U' = U \cos(\pi/16)$ against $y' = y \cos(\pi/16)$, where $\pi/16$ is

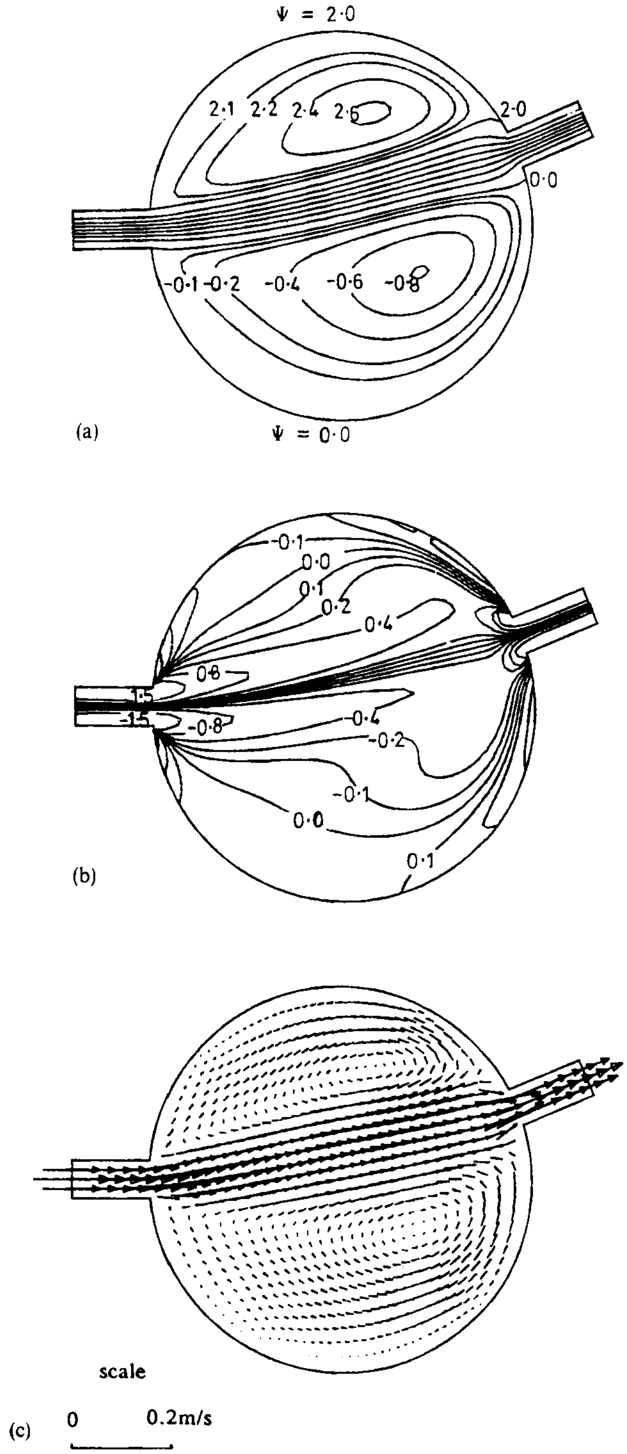

Figure 15. Predictions for $Re_l = 25$, using a 61×61 mesh, Mills' geometry: (a) stream function contours; (b) vorticity contours; (c) velocity vectors

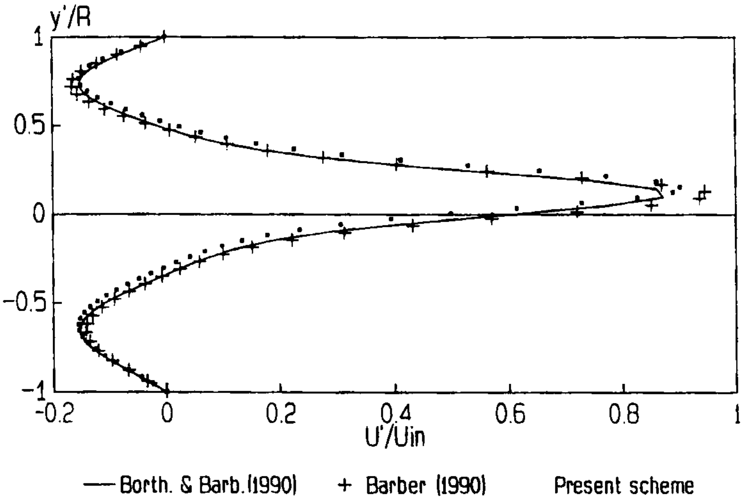

Figure 16. Velocity profiles across reservoir for $Re_I = 25$, Mills' geometry

the angle between the y-axis and the line of symmetry of the reservoir. Agreement is satisfactory everywhere, although the present scheme again shows a higher throughflow velocity than Borthwick and Barber's model.

At late times, long after reaching overall steady state, a small build up of spurious vorticity occurred close to the lower, left-hand inflexion point. At first glance, these spurious effects seemed to be somewhat anomolous; they occurred in a region where the stream function and vorticity gradients are very shallow, and the velocities are small. These could be due to an accumulation of truncation errors in the computation of vorticity values close to the points of inflexion, where extrapolation and interpolation techniques have to be applied, but the errors could not be eradicated with improved interpolation. A single pass of the spatial filter successfully eliminated the oscillations, but was not considered necessary because the effect occurred long after steady state and did not significantly disturb the flow field.

The final plots in Figure 17 show results for an inlet Reynolds number of 100, using the fine mesh. The stream function contours demonstrate that a second pair of very slow, counter rotating gyres occurs near the inlet. Additional contours of zero vorticity near the walls also indicate the presence of these gyres. Comparison with Borthwick and Barber's[36] results shows that predictions [6]obtained using the fine mesh are subject to some numerical diffusion at this Reynolds number; the secondary gyres are not as large as those obtained by the Navier–Stokes solver. Again, the vorticity plots confirm this behaviour. Even though the overall patterns agree well, the zero vorticity lines spread out further from the inlet, and around the left-hand walls, indicating smaller recirculation zones. Although the size of the secondary gyres is underpredicted, the primary gyres occupy the same locations as those given by Borthwick and Barber. The upper recirculation zone has the same strength in both cases, but the present scheme predicts a slightly weaker lower gyre. It is interesting to note that Barber's primitive-variable model also produces a weaker lower gyre (at $Re_I = 25$) than the corresponding Navier–Stokes solution. This indicates that the two boundary-fitted, depth-averaged schemes follow the same trends.

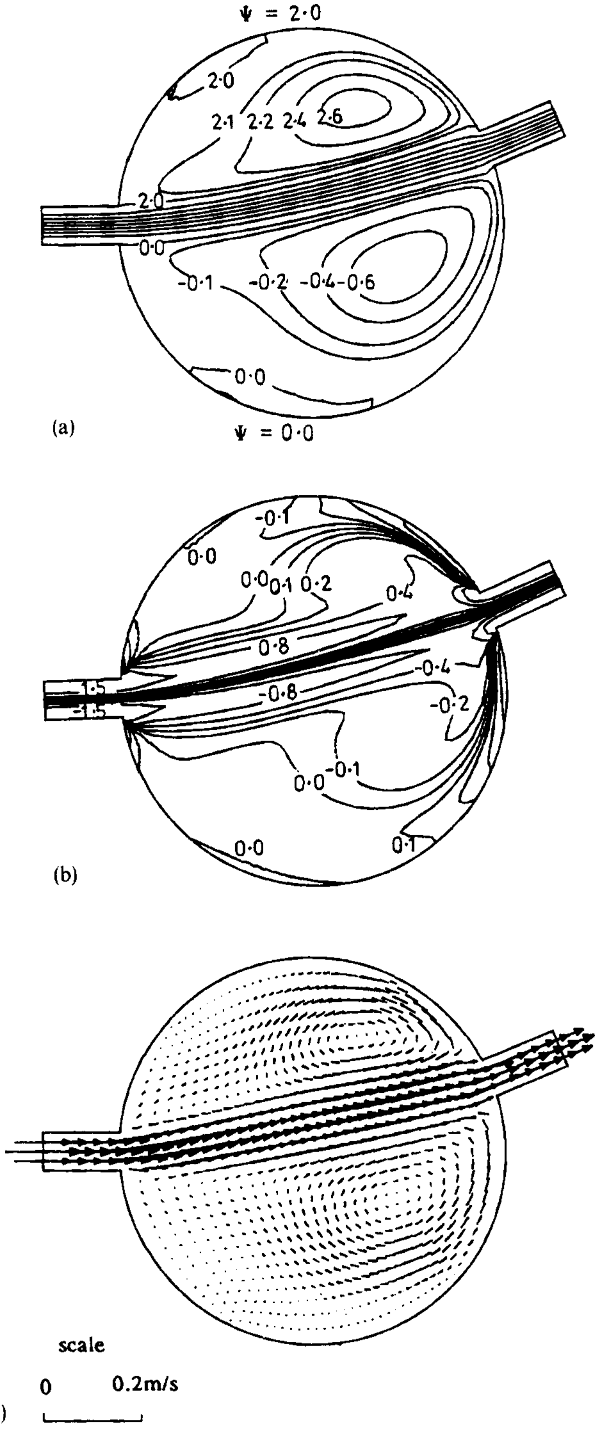

Figure 17. Predictions for $Re_l = 100$, using a 61 × 61 mesh, Mills' geometry: (a) stream function contours; (b) vorticity contours; (c) velocity vectors

CONCLUSIONS

This paper presents details of a unique non-orthogonal depth-averaged (ψ, ω) numerical model for predicting flows in shallow reservoir and river environments. It was verified against alternative semi-analytical, numerical and experimental data for laminar flow over a backward-facing step in a rectangular channel and jet-forced flow in a circular reservoir at low inlet Reynolds numbers. The results confirm that the non-orthogonal depth-averaged (ψ, ω) solver is able to predict separated, recirculating flows with reasonable accuracy.

Laminar flow past a backward-facing step was studied for inlet Reynolds numbers between 46 and 229. It is a well-documented test for the presence of artificial viscosity, and allows a simple grid to be used. Here it demonstrated that no significant artificial viscosity was introduced by the donor cell method at low Reynolds numbers below 100 using a 141 × 31 fine mesh. Second-order upwind differencing led to shorter recirculation lengths, which indicated higher levels of numerical diffusion. In order to test the performance of those additional terms related to physical mesh curvature the depth-averaged (ψ, ω) model simulated jet-forced flow in a circular reservoir. Flow separation at the inlet of the reservoir promoted large zones of recirculation, related to the non-linear advective terms in the vorticity-transport equation (therefore allowing another assessment of artificial viscosity due to upwind differencing). Although agreement with an alternative numerical scheme presented by Borthwick and Barber[36] was excellent for $10 < Re_I < 100$, at inlet Reynolds numbers less than 10 large stresses in the vicinity of corner point singularities caused oscillations which tended to destabilize the solution. At $Re_I \approx 100$, artificial viscosity became evident.

The rigid-lid condition is perhaps the major drawback of the depth-averaged (ψ, ω) model. Nevertheless, in many cases, such as lakes or reservoirs, variations in the free surface are negligible and the (ψ, ω) formulation has some possible advantages over alternative primitive variable approaches. The three variable (U, V, ζ) system is reduced to two variables which are suited to a non-staggered mesh. Moreover, the depth-averaged (ψ, ω) formulation can lead to simpler and possibly more accurate boundary conditions.

For efficient implementation on vector or parallel computers, several improvements are worth making to the numerical solution of the transformed (ψ, ω) shallow water equations. The transformed depth-averaged stream function equation is elliptic and is suited to a fast solver, such as the multigrid technique. As indicated by Wilders *et al.*,[8] the recursive solution of tridiagonal matrices in ADI schemes reduces the speed on vector computers. Consequently, a fully implicit technique, such as the preconditioned conjugate gradients method used by Wilders *et al.*, is recommended for solving the vorticity transport equation on a vector computer. Alternatively, multiprocessor architecture can be exploited in solving the transformed (ψ, ω) shallow water equations explicitly, making use of domain decomposition.

ACKNOWLEDGEMENTS

The second author (E. T. Kaar) was funded by the Science and Engineering Research Council for the duration of this work. Both authors would like to thank Dr. J. Józsa and Dr. C. Gáspár of VITUKI, Water Resources Research Centre, Hungary for checking the derivation of the (ψ, ω) equations.

APPENDIX

Coefficients in curvilinear (ψ, ω) shallow water equations

The coefficients in the non-orthogonal depth-averaged stream function equation (11) are defined as follows:

$$\sigma=\frac{1}{J}(y_\xi\delta_x-x_\xi\delta_y), \qquad \tau=\frac{1}{J}(x_\eta\delta_y-y_\eta\delta_x),$$

in which

$$\delta_x=\alpha\, x_{\xi\xi}-2\beta\, x_{\xi\eta}+\gamma\, x_{\eta\eta}, \qquad \delta_y=\alpha\, y_{\xi\xi}-2\beta y_{\xi\eta}+\gamma y_{\eta\eta},$$

$$\sigma_{\mathrm{D}}=\frac{1}{D}(\beta\, D_\xi-\gamma D_\eta) \quad\text{and}\quad \tau_{\mathrm{D}}=\frac{1}{D}(\beta\, D_\eta-\alpha\, D_\xi).$$

In the non-orthogonal depth-averaged vorticity transport equation (12) each of the effective stress terms, T_{xx}, T_{xy} and T_{yy}, is multiplied by coefficients resulting from derivative operations with respect to x and y. The only difference occurs in the definition of the various coefficients. For T_{xx} and T_{yy} they read:

$$A=x_\eta y_\eta, \qquad B=x_\xi y_\eta+x_\eta y_\xi, \qquad \Gamma=x_\xi y_\xi,$$

$$S=\frac{1}{J}(y_\xi\delta_{2x}-x_\xi\,\delta_{2y}), \qquad T=\frac{1}{J}(x_\eta\delta_{2y}-y_\eta\delta_{2x}),$$

where

$$\delta_{2x}=A\, x_{\xi\xi}-Bx_{\xi\eta}+\Gamma x_{\eta\eta}, \qquad \delta_{2y}=Ay_{\xi\xi}-B\, y_{\xi\eta}+\Gamma y_{\eta\eta},$$

$$T_{\mathrm{D}x}=\frac{x_\eta}{D}(y_\eta D_\xi-y_\xi D_\eta), \qquad T_{\mathrm{D}y}=\frac{y_\eta}{D}(x_\eta D_\xi-x_\xi D_\eta),$$

$$S_{\mathrm{D}x}=\frac{x_\xi}{D}(y_\xi D_\eta-y_\eta D_\xi), \qquad S_{\mathrm{D}y}=\frac{y_\xi}{D}(x_\xi D_\eta-x_\eta D_\xi)$$

and

$$\kappa=\frac{1}{D}\left\{A\left(D_{\xi\xi}-\frac{D_\xi^2}{D}\right)-B\left(D_{\xi\eta}-\frac{D_\xi D_\eta}{D}\right)+\Gamma\left(D_{\eta\eta}-\frac{D_\eta^2}{D}\right)+TD_\xi+SD_\eta\right\}.$$

Similarly the coefficients for T_{xy} are given by

$$\alpha_m=x_\eta^2-y_\eta^2, \qquad \beta_m=x_\xi x_\eta-y_\xi y_\eta, \qquad \gamma_m=x_\xi^2-y_\xi^2,$$

$$\sigma_m=\frac{1}{J}(y_\xi\delta_{1x}-x_\xi\delta_{1y}), \qquad \tau_m=\frac{1}{J}(x_\eta\delta_{1y}-y_\eta\delta_{1x}),$$

where

$$\delta_{1x}=\alpha_m x_{\xi\xi}-2\beta_m x_{\xi\eta}+\gamma_m x_{\eta\eta}, \qquad \delta_{1y}=\alpha_m y_{\xi\xi}-2\beta_m y_{\xi\eta}+\gamma_m y_{\eta\eta},$$

$$\tau_{\mathrm{D}m}=\frac{1}{D}(\alpha_m D_\xi-\beta_m D_\eta), \qquad \sigma_{\mathrm{D}m}=\frac{1}{D}(\gamma_m D_\eta-\beta_m D_\xi),$$

and

$$\lambda=\frac{1}{D}\left\{\alpha_m\left(D_{\xi\xi}-\frac{D_\xi^2}{D}\right)-2\beta_m\left(D_{\xi\eta}-\frac{D_\xi D_\eta}{D}\right)+\gamma_m\left(D_{\eta\eta}-\frac{D_\eta^2}{D}\right)+\tau_m D_\xi+\sigma_m D_\eta\right\}.$$

REFERENCES

1. J. J. Leendertse, 'Aspects of a computational model for long period water wave propagation' *RM-5294-PR*, The Rand Corporation, Santa Monica, California, 1967.
2. J. J. Leendertse, 'A water-quality simulation model for well mixed estuaries and coastal seas: Vol. 1, Principles of computation', *RM-6230-RC*, The Rand Corporation, Santa Monica, California, 1970.
3. J. Kuipers and C. B. Vreugdenhil, 'Calculations of two-dimensional horizontal flow', Delft Hydraulics Laboratory, *Report S163*, Part 1, The Netherlands, 1973.
4. C. B. Vreugdenhil and J. H. A. Wijbenga, 'Computation of flow patterns in rivers', *J. Hydraul. Div. ASCE*, **108(HY11)**, 1296–1310 (1982).
5. A. K. Rastogi and W. Rodi, 'Predictions of heat and mass transfer in open channels', *J. Hydraul. Div., ASCE*, **(HY3)**, 397–417 (1978).
6. J. Wolf, 'A comparison of a semi-implicit with an explicit scheme in a three-dimensional hydrodynamic model', *Continental Shelf Res.*, **2**(4), 215–229 (1983).
7. G. S. Stelling, A. K. Wiersma and J. B. T. M. Willemse, 'Practical aspects of accurate tidal computations', *ASCE J. Hydraul. Eng.*, **112**(9), 802–817 (1986).
8. P. Wilders, Th. L. van Stijn, G. S. Stelling and G. A. Fokkema, 'A fully implicit splitting method for accurate tidal computations', *Int. j. numer. methods eng.*, **26**, 2707–2721 (1988).
9. C. Taylor and J. Davies, 'Finite-element modelling of flow and dispersion in estuaries', *IAHR Symposium on River Mechanics*, Bangkok, Thailand, Paper C 39, 3, (1973).
10. R. V. Faraday, B. A. O'Connor and I. M. Smith, 'A two-dimensional finite-element model for partially mixed estuaries', *Proc. 16th Cong. IAHR*, Paper C 35, p. 3, Sao Paulo, Brazil, 1975.
11. C. Lai, 'Some computational aspects of one- and two-dimensional unsteady flow simulation by the method of characteristics', *Proc. Int. Symp. Unsteady Flow In Open Channels*, IAHR, D1-D2, 1976.
12. J. P. Benqué, J. A. Cunge, J. Feuillet, A. Hauguel and F. M. Holly, 'New method for tidal current computation', *J. Waterway, Port, Coastal Ocean Div. ASCE*, **108** (WW3), 396–417 (1982).
13. R. R. Boericke and D. W. Hall, 'Hydraulics and thermal dispersion in an irregular estuary', *J. Hydraul. Div. ASCE*, **100 (HY1)**, 85–102 (1974).
14. B. H. Johnson and J. F. Thompson, 'A discussion of boundary-fitted coordinate systems and their applicability to the numerical modelling of hydraulic problems', *Misc. Paper HL-78-9*, Mississippi State University, Vicksburg, 1978.
15. B. H. Johnson, 'VAHM—a vertically averaged hydrodynamic model using boundary-fitted coordinates', *Misc. Report HL-80-3*, Mississippi State University, Vicksburg, 1980.
16. Y. P. Sheng and J. E. Hirsh, 'Numerical solution of shallow water equations in a boundary-fitted grid', *Tech. Memo 84–15*, Aeronautical Research Associates of Princeton, Inc., Princeton, New Jersey, 1984.
17. M. L. Spaulding, 'A vertically averaged circulation model using boundary-fitted coordinates', *J. Phys. Oceanogr.*, **14**, 973–982 (1984).
18. J. B. T. M. Willemse, G. S. Stelling and G. K. Verboom, 'Solving the shallow water equations with an orthogonal coordinate transformation', *Int. Symp. on Comp. Fluid Dynamics*, Tokyo, Japan, (1985) (Reprinted as: Delft Hydraulics Communications No. 356, Jan. 1986, Delft Hydraulics Laboratory, Delft, The Netherlands.)
19. G. S. Stelling, 'On the construction of computational methods for shallow water flow problems', *Ph.D. Thesis*, Delft Univ. of Technology, The Netherlands, 1983.
20. J. H. A. Wijbenga, 'Determination of flow patterns in rivers with curvilinear coordinates', *XXI Congress of the Int. Ass. for Hyd. Research*, Melbourne, Australia. (Reprinted as: Publications No. 352, Oct. 1985, Delft Hydraulics Laboratory, Delft, The Netherlands, 1985).
21. J. Häuser, H.G. Paap, D. Eppel and A. Mueller, 'Solution of the shallow water equations for complex flow domains via boundary-fitted coordinates', *Int. j. numer. methods fluids*, **5**, 727–744 (1985).
22. R. Raghunath, S. Sengupta and J. Häuser, 'A study of the motion in rotating containers using a boundary-fitted coordinate system', *Int. j. numer. methods fluids*, **7**, 453–464 (1987).
23. A. G. L. Borthwick and R. W. Barber, 'River and reservoir flow modelling using the transformed shallow water equations', *Int. j. numer. methods fluids*, **14**, 1193–1217 (1992).
24. J. M. Hervoulet, 'Comparison of experimental data and laser measurements with the computational results of the TELEMAC code (shallow water equations)', *Proc. Int. Conf. on Interaction of Comp. Methods and Measurements in Hydraulics and Hydrology*, (1989) pp. 107–116, Dubrovnic, Yugoslavia.
25. R. B. Codell, 'Two-dimensional model of flow towards intakes', *Symposium on Modelling Techniques, ASCE*, 2, pp. 426–438, San Francisco, 1975.
26. M. L. Chalmers, 'Flow fields around estuary structures: a comparison of physical and computer models', *M.Sc. Thesis*, Univ. of Manchester, 1980.
27. D. J. Ball, R. B. S. Penoyre and B. A. O'Connor, 'Numerical modelling of the hydrodynamics of complex civil engineering structures', *Int. Conf. on Hydraulic Modelling of Civ. Eng. Structures*, Paper A2, 13–32, Coventry, 1982.
28. A. J. Oliver and A. J. Miller, 'The application of boundary-fitted coordinates to predicting 2-D flows and heat transfer in complex geometries', *Computational Techniques for Fluid Flows*, Chapter 9, 1986.
29. E. T. Kaar, 'Curvilinear systems modelling of pollutant transport in shallow waters', *D.Phil Thesis*, University of Oxford, Oxford, 1991.

30. R. A. O'Leary and T. J. Mueller, 'Correlation of physical and numerical experiments for incompressible laminar separated flows', *Project THEMIS Technical Report, UND-69-4*, Univ. of Notre Dame, Ind. Coll. of Engineering, 1969.
31. M. K. Denham and M. A. Patrick, 'Laminar flow over a downstream facing step in a two-dimensional flow channel', *Trans. Inst. Chem. Eng.*, **52,** 361–367 (1974).
32. D. J. Atkins, S. J. Maskell and M. A. Patrick 'Numerical prediction of separated flows', *Int. j. numer. methods eng.*, **15,** 129–144 (1980).
33. L. P. Hackman, G. D. Raithby and A. B. Strong, 'Numerical predictions of flows over backward facing steps', *Int. j. numer. methods fluids*, **4,** 711–724 (1984).
34. S. C. R. Dennis, 'Application of the series truncation method to two-dimensional internal flows', *Proc. 4th Int. Conf. on Numerical Methods in Fluid Dynamics*, Univ. of Colorado, Springer, 1974, pp. 146–151.
35. R. W. Barber, 'Numerical modelling of jet-forced circulation in reservoirs using boundary-fitted coordinate systems', *Ph.D. Thesis*, University of Salford, 1990.
36. A. G. L. Borthwick and R. W. Barber, 'Prediction of low Reynolds number jet-forced flow inside a circle using the Navier–Stokes equations', *Int. J. Eng. Fluid. Mech.*, **4**(3), 323–343 (1990).
37. R. D. Mills, 'Computing internal viscous flow problems for the circle by integral methods', *J. Fluid Mech.*, **79**(3), 609–624 (1977).